Article:
Chen, C., Wang, J., Algeo, T.J. et al. (5 more authors) (2024) Application of pyrite trace-metal and S and Ni isotope signatures to distinguish sulfate- versus iron-driven anaerobic oxidation of methane. Chemical Geology, 662. 122211. ISSN 0009-2541

https://doi.org/10.1016/j.chemgeo.2024.122211

Application of pyrite trace-metal and S and Ni isotope signatures to distinguish sulfate- versus iron-driven anaerobic oxidation of methane

Can Chen[1,2], Jiasheng Wang[1,2]*, Thomas J. Algeo[2,3,4], Jian-Ming Zhu[5], Simon W. Poulton[6], Zhou Wang[1,2], Cong Cheng[1,7], Qiang Song[1,2]

[1] *Hubei Key Laboratory of Marine Geological Resources & College of Marine Science and Technology, China University of Geosciences, Wuhan, 430074 China*

[2] *State Key Laboratory of Biogeology and Environment Geology, China University of Geosciences, Wuhan, 430074 China*

[3] *State Key Laboratory of Geological Processes and Mineral Resources, China University of Geosciences, Wuhan, 430074 China*

[4] *Department of Geosciences, University of Cincinnati, Cincinnati, OH, 45221 USA*

[5]*State Key Laboratory of Isotope Geochemistry, Institute of Earth Sciences, China University of Geosciences, Beijing, 100083 China*

[6]*School of Earth and Environment, University of Leeds, Leeds LS2 9JT, UK*

[7]*Institute for Advanced Marine Research, China University of Geosciences, Guangzhou, 510075, China*

Corresponding author email: js-wang@cug.edu.cn *(J. Wang)*

Abstract: The formation of authigenic pyrite in marine sediments involves multiple reactions between ferrous iron (Fe^{2+}) and hydrogen sulfide (H_2S). Ferrous iron is commonly provided through the reductive dissolution of Fe-(oxyhydr)oxides by organic matter (i.e., dissimilatory Fe reduction), dissolved sulfide (i.e., abiotic Fe reduction) or methane (i.e., Fe-AOM), whereas sulfide is supplied by organoclastic sulfate reduction (OSR) or sulfate-driven anaerobic oxidation of methane (SD-AOM). Since Rayleigh-type distillation operates widely in sediments of gas-hydrate-bearing zones, sulfur and nickel isotope compositions (i.e., $\delta^{34}S$ and $\delta^{60}Ni$) cannot readily distinguish OSR- from SD-AOM-associated pyrite. However, these microbial pathways may yield different patterns of trace-element enrichment in pyrite. To better understand the linkage of trace-element patterns to specific microbial pathways (i.e., Fe reduction, Fe-AOM, OSR and SD-AOM), and to evaluate the use of S and Ni isotopic signatures as tracers for pyrite formation pathways in methane-rich sediments, we report pyrite-associated trace element and $\delta^{34}S$ and $\delta^{60}Ni$ isotope analyses of sediments from a gas hydrate borehole (Site GMGS4-SC-03) from the Shenhu area, Pearl River Mouth Basin, South China Sea. Pyrite formed in conjunction with Fe- and/or SD-AOM exhibits abundant framboidal overgrowths and extremely high $\delta^{34}S$ (up to +142.8‰) and $\delta^{60}Ni$ (up to +2.72‰), representing the highest stable S and Ni isotopic compositions of pyrite reported to date. These pyrite morphologies are enriched in Co and Ni, which may be a diagnostic signature of an SD-AOM pathway. By contrast, OSR-associated pyrite is enriched in Cu and Zn due to OSR-induced release of trace elements from decaying organic matter. In addition, the relationship of As to Cu and/or Zn can distinguish microbial Fe/Mn reduction from Fe/Mn-AOM, because microbial Fe/Mn reduction releases trace elements from both Fe/Mn-(oxyhydr)oxides (i.e., As) and organic matter (i.e., Cu and Zn), whereas Fe/Mn-AOM only releases trace elements from Fe/Mn-(oxyhydr)oxides. Furthermore, an observed covariation

between As and either Co or Ni in most pyrite with high $\delta^{34}S$, indicates that this pyrite captured both As released during Fe/Mn-AOM and Co and Ni from SD-AOM. Thus, the high nickel isotope values measured in this study likely dominantly reflect release of isotopically heavy Ni from Fe- and Mn-(oxyhydr)oxides. Our results demonstrate that the trace-element composition of pyrite in gas-hydrate-bearing sediments can record the geochemical signature of the dominant microbial processes.

Keywords: South China Sea; sulfur isotopes; nickel isotopes; arsenic; hydrogen sulfide; AOM

1. Introduction

Pyrite is stable in anoxic sediments on geological timescales, and therefore authigenic pyrite can provide information on biogeochemical pathways during early diagensis (e.g., Lin-Q et al., 2016; Lin-Z et al., 2016; Liu et al., 2022). The sulfide required for authigenic pyrite formation can be generated through both organoclastic sulfate reduction (OSR) and sulfate-driven oxidation of methane (SD-AOM). In turn, distinguishing pyrite related to OSR versus SD-AOM can help to identify paleo-methane release events, and can also provide useful insight into relationships between hydrate stability, the global carbon cycle, and climate (e.g., Hesselbo et al., 2000; Berner, 2002; Jiang et al., 2003; Wang et al., 2008; Chen et al., 2023).

Numerous studies have been dedicated to examining the fingerprints resulting from different formation pathways of authigenic pyrite. The sulfur isotopic composition of pyrite is one of the most frequently utilized proxies, because OSR preferentially partitions ^{32}S into the sulfide pool, leaving the sulfate pool that is used in SD-AOM enriched in ^{34}S (e.g., Jørgensen et al., 2004, 2006; Peketi et al., 2012; Borowski et al., 2013; Lin-Q et al., 2016; Lin-Z et al., 2016; Feng et al., 2018). In addition,

Chen et al. (2023) found that pyrite formed in conjunction with SD-AOM can contain higher concentrations of Co and Ni, with lower δ^{60}Ni values than those formed via OSR, due to Ni uptake and isotopic fractionation by SD-AOM. These pyrite-associated proxies have the potential to identify ancient methane-release events.

However, due to potential changes in sedimentation rate, pyrite isotopic proxies may not be as reliable an indicator of SD-AOM-related processes as once thought (e.g., Pasquier et al., 2017; Liu et al., 2021). Increased sedimentation rates result in sediment porewaters becoming closed systems more rapidly, effectively decreasing the exchange of sulfate between porewaters and the overlying water column. When this occurs, porewaters can become ^{34}S enriched more rapidly, resulting in an increase in pyrite δ^{34}S compositions independent of the sulfate reduction pathway (Pasquier et al., 2017; Liu et al., 2021). It should be noted in this context that the formation of gas hydrates, which can lead to significant production of SD-AOM-related pyrite, is often closely linked to increased sedimentation rates. This is because elevated sedimentation rates not only serve as a protective mechanism for organic matter against aerobic oxidation, thereby allowing enhanced methane production in the methanogenic zone (Claypool and Kaplan, 1974; Borowski, 2004; Su et al., 2012; Chen et al., 2013), but also tend to result in an undercompacted area that constitutes a good fluid migration system (Yu et al., 2012, 2014). However, Ni isotope and pyrite-trace-element signatures linked to SD-AOM have been established in a setting characterised by a consistent, low sedimentation rate with no visible gas-hydrate (Chen et al., 2023).

To evaluate the feasibility of utilizing these proxies as tracers for SD-AOM in methane-rich sediments, we report an investigation of pyrite trace element concentrations, in addition to δ^{34}S and δ^{60}Ni compositions, at Site GMGS4-SC-03 (hereafter shortened to “Site SC03”; Fig. 1), which is a

gas hydrate drilling site in the Shenhu area, Pearl River Mouth Basin (PRMB), South China Sea. This site has been strongly affected by mass transport deposits (MTD) and is characterized by variable and high sedimentation rates, with multiple submarine canyons (Yu et al., 2012; Cheng et al., 2020; He et al., 2022). In addition, Fe/Mn-driven anaerobic oxidation of methane (Fe/Mn-AOM) prevails in this area (Liu et al., 2018; Xie et al., 2019), and therefore we also examine how this early diagenetic process affects geochemical signatures.

2. Geological setting

The Pearl River Mouth Basin (PRMB) is the largest Cenozoic petroliferous basin in the northern South China Sea, and is located on the continental shelf to slope, covering an area of about 19.38×10^4 km^2 (He et al., 2017). Since the Eocene, the PRMB has undergone three major geological stages: The pre-rifting stage (pre-Cenozoic) represents the formation of the basement, comprising granites, sedimentary and metamorphic rocks; during the syn-rifting stage (Eocene) the basin was dominantly lacustrine; during the post-rifting stage (Oligocene to present) marine conditions occurred (Fig. 2) (Gong et al., 2013; He et al., 2017; Mi et al., 2018). Since the Oligocene, numerous submarine canyons, which show characteristics of unidirectional migration under the influence of contour currents, developed at the margin of the northern shelf of the South China Sea (Zhu et al., 2010; Gong et al., 2013; He et al., 2013). The Dongsha event, which resulted in an increased detrital input to the area from the Dongsha uplift, is considered to have resulted in elevated sedimentation rates since the Late Miocene (Yu et al., 2012, 2014).

3. Materials and methods

3.1. Study site

Expedition GMGS4 took place in 2016 on the geotechnical drilling vessel Fugro Voyager. Locally, the study area is characterized by a migrating canyon system (Sun et al., 2018; Fig. 1B). Site SC03 (water depth 1310 m) was drilled through the inferred gas hydrate zone (Fig. 1C; i.e., 0–225 mbsf) and consists of marine shales with interbedded sand. Although there is no detailed age model for this drillcore, the study interval approximately encompasses the mid-Pliocene to the present, based on correlation of seismic horizons (T0–T30 in Figs. 1C and 2; Cheng et al., 2020). In addition, the study site is likely to have been affected by increased sedimentation rates since the Late Miocene, because (1) the Late Miocene Dongsha event provided more detrital input to the study area from the Dongsha uplift (Yu et al., 2012, 2014), (2) a sharp increase in average sedimentation rate has been found in a nearby site from ~3 Ma to the present (Fig. 2; Tian et al., 2008), and (3) the study area has been affected by the development of submarine canyons since the Oligocene (Sun et al., 2018), with significantly higher sedimentation rates in the canyons relative to their flanks (Paradis et al., 2018).

3.2. Sample preparation and scanning electron microscope observations

Marine shale samples were stored at ~4 °C in shipboard and onshore laboratories. Samples were processed in the State Key Laboratory of Biogeology and Environmental Geology at the China University of Geosciences-Wuhan, according to the following procedure: (1) approximately 15 cm^3 of sediment was air-dried in a 40 °C oven for 24 h and then weighed; (2) half of the dried sediment was prepared for whole-rock analysis and the other half was used to extract pyrite; and (3) authigenic pyrite crystals were identified and handpicked using a high-power binocular microscope (Carl Zeiss Stemi 2000-C). Scanning electron microscope observations of the handpicked pyrite aggregates were

133 undertaken using an FEI Quanta 450 FEG at the State Key Laboratory of Geological Processes and
134 Mineral Resources of the China University of Geosciences-Wuhan.
135
136 *3.3. Major-element analysis*
137 Major element concentrations for 22 bulk samples were analyzed on a Zsx Primus II wavelength
138 dispersive X-ray fluorescence spectrometer at the Wuhan Sample Solution Analytical Technology Co.,
139 Ltd., Wuhan, China. These data were calibrated using the national standard materials GBW07101-14,
140 GBW07401-08 and GBW07302-12, and corrected by the theoretical α coefficient method (Lachance
141 and Claisse, 1995), yielding relative standard deviations of less than 2% for all elements of interest.
142
143 *3.4. Trace-element analysis*
144 A total of 22 bulk samples were analyzed on an Agilent 7700e ICP-MS at the Wuhan Sample
145 Solution Analytical Technology Co., Ltd., Wuhan, China. One mL of HNO_3 and 1 mL of HF were
146 slowly added to 50 mg of sample powder (200 mesh) in a Teflon bomb, and heated to 190 °C in an
147 oven for >24 h. After cooling, the Teflon bomb was opened and placed on a hotplate at 140 °C and
148 evaporated to incipient dryness, and then 1 mL of HNO_3 was added and evaporated to dryness again.
149 One mL of HNO_3, 1 mL of MQ water, and 1 mL of internal standard solution of 1 ppm In were added,
150 and the Teflon bomb was resealed and placed in the oven at 190 °C for >12 h. The final solution was
151 transferred to a polyethylene bottle and diluted to 100 g by the addition of 2% HNO_3 for ICP-MS
152 analyses. The international rock standards BHVO-2, RGM-2, GSR-3 and JA-2 were used to monitor
153 analytical accuracy. Analytical precision was better than ± 5%.
154 Enrichment factors for Ni (Ni_{EF}) were calculated by normalizing to Post-Archean Australian

Shale (PAAS; Taylor and McLennan, 1985) as:

$$Ni_{EF} = (Ni/Al)_{sample}/(Ni/Al)_{PAAS} \quad (1)$$

We also monitor the Eu anomaly (Eu/Eu*) to examine whether our samples have been affected by hydrothermal activity, where Eu/Eu* is calculated using the formula (Lawrence et al., 2006):

$$Eu/Eu^* = Eu_N/(Sm_N^2 \times Tb_N)^{1/3} \quad (2)$$

where subscript N represents elements normalized to PAAS. Middle-REE anomalies (MREE/MREE*; MREEs consisting of Sm, Eu, Gd, Tb, Dy and Ho) were calculated using the formula (Chen et al., 2015):

$$MREE/MREE^* = \frac{2 \times average(MREE)}{average(LREE)+average(HREE)} \quad (3)$$

where LREE represents light REEs (La, Ce, Pr and Nd), and HREE represents heavy REEs (Er, Tm, Yb and Lu). All REEs were normalized to PAAS.

Biogenic Ba (Ba_{bio}), as an indicator of primary productivity, was calculated as:

$$Ba_{bio} = Ba_{sample} - Al_{sample} \times (Ba/Al)_{detr} \quad (4)$$

Compilations of crustal composition data yield $(Ba/Al)_{detr}$ ratios between 0.005 and 0.010 (e.g., Taylor and McLennan, 1985), which have been used in many studies (Dymond et al., 1992; Bonn et al., 1998; Prakash Babu et al., 2002). However, a substantial fraction of Ba in detrital sediments appears to be lost during weathering and transport in the terrestrial environment, yielding siliciclastic $(Ba/Al)_{detr}$ ratios around 0.002–0.004 upon deposition in marine systems (Rutsch et al., 1995; Reitz et al., 2004). Thus, commonly used $(Ba/Al)_{detr}$ ratios based on average upper crustal compositions may overestimate $(Ba/Al)_{detr}$. Here, we use an approach based on estimating $(Ba/Al)_{detr}$ ratios from Al vs. Ba crossplots, in which the majority of samples above a line that passes through the origin is assumed to represent the detrital component of Ba and assuming the samples with the lowest Ba/Al ratios contain no biogenic barium (Shen et al., 2015; Schoepfer et al., 2015). This method yielded a 0.005

178 $(Ba/Al)_{detr}$ ratio for our study units (Fig. S1), which as expected is lower than the overestimated
179 average upper crustal $(Ba/Al)_{detr}$ ratio.

180 A total of 104 samples of handpicked pyrite were analyzed by LA-ICP-MS at the Wuhan Sample
181 Solution Analytical Technology Co., Ltd., Wuhan, China. Laser sampling was performed using a
182 GeolasPro laser ablation system that consists of a COMPexPro 102 ArF excimer laser (wavelength
183 of 193 nm and maximum energy of 200 mJ) and a MicroLas optical system. An Agilent 7700e ICP-
184 MS instrument was used to acquire ion-signal intensities. Helium was utilized as a carrier gas. Argon
185 was used as the make-up gas and mixed with the carrier gas via a T-connector before entering the
186 ICP-MS. A "wire" signal smoothing device was included in this laser ablation system. The spot size
187 and frequency of the laser were set to 32 μm and 5 Hz, respectively. The trace-element compositions
188 of sulfides were calibrated against reference materials NIST 610 and NIST 612. A sulfide reference
189 material (MASS-1 from the USGS) was used as an unknown to verify the accuracy of the calibration
190 method. Each analysis incorporated a background acquisition time of ~20-30 s followed by a 50-s
191 data acquisition time. The Excel-based software ICPMSDataCal was used to perform offline selection
192 and integration of background and analyzed signals, time-drift corrections, and quantitative
193 calibrations of trace-element analyses. The uncertainties (2σ) for trace-element concentrations are
194 listed in Table S1.

195

196 *3.5. Pyrite sulfur isotopic analysis*

197 The stable sulfur isotopic compositions of handpicked pyrite were analyzed using a Delta V Plus
198 continuous flow isotope ratio mass spectrometer coupled to an elemental analyzer (EA-IRMS) at
199 State Key Laboratory of Biogeology and Environmental Geology. All results are reported here in

standard delta notation as per mille deviations from Vienna-Cañon Diablo Troilite (VCDT). Measurement errors of ~0.2‰ (2σ) for pyrite $\delta^{34}S$ were calculated from replicate analyses of IAEA international standards: IAEA S1 (−0.3‰), IAEA S2 (+22.7‰) and IAEA S3 (−32.3‰).

3.6. Nickel purification and isotopic analysis

Nickel purification and isotopic analyses were undertaken at the State Key Laboratory of Isotope Geochemistry, China University of Geosciences (Beijing). Seven samples of ≥ 30 μm pyrite were selected for Ni-isotope analysis. Before Ni purification, 600 to 800 ng of Ni in each sample aliquot was mixed with a ^{61}Ni-^{62}Ni double spike in 15 mL PFA beakers according to the optimized ratio of $^{62}Ni_{spike}/^{58}Ni_{sample}$ = 1.35 (Wu et al., 2019). The sealed beakers were placed on a hotplate overnight at 80 °C to equilibrate the double spike and samples. Subsequently, the sample-spike mixed solution was evaporated to dryness at 110 °C and immediately dissolved in 0.1 mL of 0.5 M HCl and, after cooling, 0.5 mL of 10.5 M HCl was added. The resulting 0.6 mL of 8.75 M HCl sample solution was then loaded onto columns. Samples were purified for high-precision measurement of Ni isotopes through a four-step procedure using five chromatographic columns in a Class 100 hood, as per the procedure of Wu et al. (2019).

Nickel isotopes were measured on a Neptune Plus MC-ICP-MS equipped with 9 Faraday cups with feedback amplifiers with corresponding 10^{11} Ω resistors. In the static mode, Faraday cups L3, L2, C, H1, H2 and H4 were used to collect ^{57}Fe, ^{58}(Ni, Fe), ^{60}Ni, ^{61}Ni, ^{62}Ni and ^{64}Ni, respectively. Sample solutions containing 30 μg/L of Ni in 2% HNO_3 were introduced into the plasma via a desolvator (the improved Aridus II with an ice chamber; Wu et al., 2020) coupled with a micro-concentric PFA nebulizer (ESI Scientific, 100 μL/min). Platinum cones (i.e., an H sample and an X

skimmer cone) were employed, and the signal intensities of ^{60}Ni were approximately 7 V for samples, while the baseline for ^{60}Ni was less than 2 mV in an N_2 atmosphere. Thus, the contribution of the blank baseline to our Ni isotope analyses was negligible. The spiked standard SRM 986 was analyzed before and after every 3 samples to monitor instrument stability. Data reductions were performed using an offline iterative Excel Worksheet program. Ni isotope ratios are reported in delta (δ) notation as per mille (‰) deviations relative to SRM 986 (i.e., $\delta^{60}Ni$ (‰) = $[(^{60}Ni/^{58}Ni)_{sample} / (^{60}Ni/^{58}Ni)_{SRM986} - 1) \times 1000$), and all reported $\delta^{60}Ni$ values were normalized to the average of bracketing SRM986 standards that were determined immediately before and after the sample analyses, using $\delta^{60}Ni_{corrected\text{-}sample} = \delta^{60}Ni_{sample} - \delta^{60}Ni_{SRM986}$ (Wu et al., 2022).

4. Results

4.1. General geochemistry of bulk sediments

Gas hydrate concentrations at Site SC03 have previously been calculated from methane mass balance in pressure core samples and porewater chloride freshening anomalies (Yang et al., 2017), and are inferred to increase from 130 mbsf to 225 mbsf, with a mean of 37% of pore volume (Fig. 3A). The depth of the gas hydrate zone coincides with anomalies in the electrical resistivity and sonic velocity downhole logs (Yang et al., 2017; Zhang et al., 2020). The presence of a gas chimney developed along a deep fault at Site SC03 (Cheng et al., 2020) as well as a crossplot of $C_1/(C_2+C_3)$ versus $\delta^{13}C\text{-}C_1$ from the nearby site W17 (~2 km away) indicate that the source of the gas is dominated by deep thermogenic methane (Ren et al., 2023).

Clay contents (proxied by Al_2O_3) exhibit a generally increasing trend from shallow to deep depths, with values of 10.9 wt% at 45.2 mbsf and 15.3 wt% at 216.7 mbsf (Table S2, Fig. 3B). The trace

244 elements Co, Ni, Cu and Zn, which may be related to SD-AOM or OSR (Smrzka et al., 2020; Chen
245 et al., 2023), covary with Al_2O_3 concentrations (Table S3, Fig. 3). Y/Ho ratios range from 25.5 to 28.2,
246 with a mean of 26.9 (Table S3), which is close to PAAS (Y/Ho = 27.2) Thus, as described above,
247 PAAS was used to calculate Ni_{EF} values, which ranged from 0.76 to 0.86, with a mean of 0.82 (Fig.
248 3E; Table S3). Excluding two outliers with exceptionally high Ba_{bio} values (Fig. 3G open circles), the
249 remaining samples exhibit a strong relationship between Ba and Al (Fig. S1; $r = +0.90$, $p < 0.01$, $n =$
250 20), and a gradual decrease in Ba_{bio} concentrations occurs, from 64.3 ppm at 50.2 mbsf to 2 ppm at
251 216.7 mbsf, while Mn × Co generally shows an increase, from 0.41 at 45.2 mbsf to 1.04 at 216.7
252 mbsf (Fig. 3H; Table S3).
253 The REE/PAAS compositions of all samples exhibit a slight enrichment in middle REEs (Fig. 4).
254 In addition, MREE/MREE* ratios range from 8.9 to 9.7, with a mean of 9.3. Eu/Eu* ratios range
255 from 0.99 to 1.08, with a mean of 1.04 (Table S3). These ratios do not exhibit any discernible changes
256 with depth (Fig. S2) or with clay content, as proxied by Al_2O_3 (Fig. S3).
257
258 *4.2. Pyrite morphology and S-isotopes*
259 To ensure that all sampled pyrite was authigenic, scanning electron microscope (SEM)
260 observations were used as evidence of authigenic characteristics. The pyrite grains in the study units
261 are mainly (>70%) rods or cylinders that were recovered as broken segments (0.2–2.0 mm long) of
262 originally more elongated features (Fig. 5A), while a smaller pyrite fraction consists of irregular
263 masses of framboids (Fig. 5B). Although some pyrite grains appear massive, the majority consist of
264 aggregates of small framboids (with diameters ranging from 5 to 50 μm, averaging 10-20 μm) when
265 viewed on the broken surfaces. In addition, the radial overgrowths surrounding the framboidal

nucleus can be observed through the broken framboids (Fig. 5C-F). Some framboids exhibit overgrowths that are nearly as wide as their nucleus diameter (Fig. 5C-E), while others display relatively narrower or no overgrowth (Fig. 5F-H).

The $\delta^{34}S$ values of pyrite exhibit a wide range, spanning from -40.4 to +142.8‰ (Table 1). These $\delta^{34}S$ values show no discernible trend with depth, as each adjacent interval displays both positive (> +20‰) and negative (< –20‰) $\delta^{34}S$ values (Fig. 6A). It is noteworthy that a single pyrite aggregate at 150.2 mbsf exhibits an exceptionally high $\delta^{34}S$ value (reaching up to +142.8‰), representing the highest stable sulfur isotope composition of pyrite reported to date, surpassing the value of +114.8‰ documented by Lin-Z et al. (2016). Comparing $\delta^{34}S$ values with the corresponding scanning electron microscope images, we find that framboids with thicker overgrowths generally exhibit higher $\delta^{34}S$ values (Fig. 5C-E), while framboids with no or relatively thinner overgrowths exhibit lower $\delta^{34}S$ values (Fig. 5F-H).

4.3. Nickel concentrations and isotopes in pyrite

Seven pyrite aggregates were chosen for nickel purification and analysis of Ni isotopes (Fig. 6B; Table 2). With the exception of one sample at 50.2 mbsf with relatively low $\delta^{60}Ni$ (+0.69‰), all other samples exhibit high $\delta^{60}Ni$ values ranging from +1.98 to +2.72‰, and the highest $\delta^{60}Ni$ value in this study (+2.72‰) represents the highest nickel isotopic composition reported to date, surpassing the value of +2.47‰ from a ferromanganese crust documented by Gall et al. (2013). The Ni concentrations that were measured during the $\delta^{60}Ni$ analyses show a generally increasing trend from 162 ppm at 50.18 mbsf to 790 ppm at 216.70 mbsf (Fig. 6D, red stars; Table 2).

4.4. Trace-element concentrations in pyrite

The trace-element concentrations in pyrite are shown in Table 3 and Fig. 6, and uncertainties (2σ) are given in Table S1. Although the selected trace elements (Co, Ni, Cu, Zn and As) exhibit no discernible correlation with depth (Fig. 6) or their bulk-rock chemistry (Fig. S4), the enrichment patterns of Co, Ni, Cu and Zn appear linked to pyrite $\delta^{34}S$ compositions. Co and Ni exhibit preferential enrichment in high-$\delta^{34}S$ pyrite, whereas Cu and Zn display enrichment in low-$\delta^{34}S$ pyrite (Fig. 6C-F). For As, samples above 180 mbsf are enriched in low-$\delta^{34}S$ pyrite, but below 180 mbsf, enrichments are observed in high-$\delta^{34}S$ pyrite (Fig. 6G). The behavior of Co, Ni, Cu and Zn in pyrite is more clearly observed via crossplots of pyrite trace element concentrations versus $\delta^{34}S$ (Fig. 7). Nickel exhibits a stronger positive correlation ($r = +0.72$, $p < 0.01$, $n = 110$) with $\delta^{34}S$ relative to Co ($r = +0.51$, $p < 0.01$, $n = 104$) (Fig. 7A-B).

5. Discussion

5.1. Early diagenetic zonation

The geochemistry of authigenic pyrite is controlled by early diagenetic reactions. Here, we assign numerical designations to these zones at Site SC03 (i.e., from oxic to methanogenic zones; Table 4) to facilitate discussion. Organic matter undergoes oxidation through a series of processes, starting at the sediment-water interface and progressing downwards into the sediment, facilitated by oxygen and nitrate (Zone I), Fe/Mn-(oxyhydr)oxides (Zone II), and sulfate (Zone III). Nearly all upward-fluxing methane from the methanogenic and/or gas-hydrate-bearing zone (Zone VI) is consumed through SD-AOM (Zone IV; Table 4). While these zones overlap, and thus, for example, sulfide can be generated in the zone of Fe/Mn reduction (Canfield, 1989; Krom et al., 2002), their description relates to the

310 dominant process occurring in each zone (e.g., Canfield and Thamdrup, 2009). Thus, the reductive
311 dissolution of Fe/Mn-(oxyhydr)oxides by abiotic reaction with dissolved sulfide (e.g., Canfield, 1989;
312 Poulton et al., 2004), may occur in micropores in any zone where sulfide is generated, including in
313 the zone of Fe/Mn reduction (e.g., Canfield, 1989; Krom et al., 2002). In particular, however, if
314 reactive Fe (oxyhydr)oxides are not sufficiently reduced in Zone II, they can be buried more deeply,
315 where they may react with additional H_2S or upwelling methane. Thus, abiotic Fe reduction may
316 occur in Zones II-IV, while Fe/Mn-AOM may occur at any depth below Zone II (e.g., Zone V, as
317 given in Table 4).
318
319 *5.2. Pyrite $\delta^{34}S$ values linked to pyrite morphology*
320 The OSR and SD-AOM processes can be distinguished at Site SC03 based on pyrite $\delta^{34}S$, as
321 OSR preferentially partitions ^{32}S into the sulfide pool (Zone III), leaving the sulfate pool that is used
322 in SD-AOM enriched in ^{34}S (Zone IV) (e.g., Canfield, 2001; Neretin et al., 2004; Peketi et al., 2012).
323 However, recent studies have revealed that authigenic pyrite $\delta^{34}S$ records a mixed signal from OSR
324 and SD-AOM (Lin-Z et al., 2016; Liu et al., 2020; Chen et al., 2023). Measurements of $\Delta^{33}S$ (where
325 $\Delta^{33}S = \delta^{33}S - 1000 \times [(1 + \delta^{34}S/1000)^{0.515} - 1]$; Ono et al., 2006) can efficiently reflect this
326 phenomenon, because mixtures of pyrite generated by OSR and SD-AOM exhibit intermediate $\delta^{34}S$
327 values but have a $\Delta^{33}S$ signature that is lower than that of either endmember, due to non-linear mixing
328 effects (Ono et al., 2006). $\Delta^{33}S$-$\delta^{34}S$ crossplots show a mixing line connecting these two endmembers
329 (Lin et al., 2017; Liu et al., 2020). In addition, Lin-Z et al. (2016) applied secondary ion mass
330 spectroscopy to analyze pyrite framboid $\delta^{34}S$ compositions and found an increase in $\delta^{34}S$ values from
331 the framboidal nucleus to the overgrowth layers. This observation suggests that SD-AOM facilitated

the formation of later-stage pyrite overgrowths with elevated $\delta^{34}S$ values compared to the initial framboidal nucleus formed through OSR.

Pyrite overgrowths usually become more abundant at greater depths during the later stages of pyritization (e.g., Ohfuji and Rickard, 2005; Taylor and Macquaker, 2011), whereas the nucleus of framboids is considered to result from relatively rapid nucleation or crystal growth under high supersaturation to form mackinawite (FeS) and/or greigite (Fe_3S_4) intermediates (e.g., Wilkin and Barnes, 1996; Butler and Rickard, 2000; Rickard and Luther, 2007). The development of larger overgrowths or euhedral pyrite is typically found in seepage settings, where the continuous supply of methane leads to rapid consumption of sulfate in shallow sediments, resulting in lower levels of sulfide saturation at depth (Lin-Z et al., 2016). Thus, exceptionally large, framboids can result from overgrowths linked to the SD-AOM process in the sulfate-methane transition zone (Lin-Q et al., 2016) .

Consistent with this hypothesis, we observed that pyrite with larger overgrowths on framboidal nuclei usually exhibit higher $\delta^{34}S$ values at Site SC03 (Fig. 5). We utilized the ratio of overgrowth thickness to total framboid diameter (i.e., framboidal nucleus plus overgrowth thickness), which we term "overgrowth fraction", as a measure of the proportion of overgrowth within individual framboids that were sufficiently intact. Due to the prevalence of broken pyrite grains (e.g., Fig. 5C, F), values of overgrowth fraction could not be determined for all samples. Nevertheless, we measured overgrowth fractions for 203 framboids in 20 samples (Table S4; Fig. 8). A strong relationship is apparent between $\delta^{34}S$ composition and overgrowth fractions (Fig. 8; $r = +0.94$, $p < 0.01$, $n = 20$). This demonstrates that increased pyrite $\delta^{34}S$ values are mainly the result of development of later-formed, AOM-caused overgrowths, suggesting that the dominant formation pathways (OSR or SD-

AOM) of pyrite may be distinguished by their $\delta^{34}S$ values.

5.3. High pyrite nickel and sulfur isotope signatures

As mentioned above, the peak Ni and S isotopic values at Site SC03 ($\delta^{60}Ni$ = +2.72‰ and $\delta^{34}S$ = +142.8‰) appear to represent the heaviest compositions reported (to the best of our knowledge), surpassing published values of $\delta^{60}Ni$ = +2.47‰ (Gall et al., 2013) and $\delta^{34}S$ = +114.8‰ (Lin-Z et al., 2016), respectively. The average $\delta^{60}Ni$ composition of seawater is +1.44‰, with negligible variability across different ocean basins (Cameron and Vance, 2014). Additionally, the preferential uptake of isotopically light Ni by Ni-sulfides ($\Delta^{60}Ni_{Ni(HS)^+-Ni^{2+}}$) results in a fractionation of approximately –0.66‰ at 25°C (Fujii et al., 2014; Vance et al., 2016). Consequently, in the absence of any other biological fractionation, the expected $\delta^{60}Ni$ value for pyrite would be around +0.78‰, which aligns with our sample obtained at 50.2 mbsf ($\delta^{60}Ni$ = +0.69‰). At Site SC03, the extremely high $\delta^{60}Ni$ values at 92.5–216.7 mbsf ($\delta^{60}Ni$ = +1.98 to +2.72‰) indicate that there were additional diagenetic processes contributing to ^{60}Ni-enrichment. Possible explanations for this, which we consider in more detail below, include: (1) fractionation occurring during processes contributing to the oceanic inputs of Ni, (2) biologically mediated fractionation of Ni in seawater/porewater, (3) Rayleigh-type distillation between porewater and pyrite, (4) additional release of Ni to porewater with high $\delta^{60}Ni$, or (5) a combination of these factors, as the scenarios are not mutually exclusive.

For the first potential explanation, reflecting variability in isotopic fractionation during processes contributing to the oceanic inputs of Ni, the main sources are continental weathering and hydrothermal fluids. The world's major rivers are more enriched in heavy isotopes than the continental rocks from which Ni was derived (Cameron and Vance, 2014), possibly due to oxidation

376 of Fe^{2+} released from bedrock and subsequent precipitation, resulting in the retention of a light pool
377 of Ni in solid weathering products (Spivak-Birndorf et al., 2018). Although terrigenous inputs
378 increased in the interval of high δ^{60}Ni (Fig. 3B), this increase is insufficient in isolation to account
379 for pyrite δ^{60}Ni values as high as +2.72‰, because δ^{60}Ni values for the world's major rivers are much
380 lower, e.g., +0.29 to +1.34‰, with a mean of +1.27‰ in the Changjiang, the main source to this
381 region of the South China Sea (Cameron and Vance, 2014). The fluid fluxes from hydrothermal vents
382 associated with mid-ocean ridges are estimated to introduce up to 20% of the yearly input of dissolved
383 Ni to the ocean (Gall et al., 2013), making it a major source. However, the absence of a discernible
384 Eu anomaly in the study samples (Eu/Eu* = 0.99-1.08) argues against this possibility.

385 In seawater, Ni concentrations commonly correlate with major nutrients, such as silicon and
386 phosphorus, suggesting that Ni behaves as a micronutrient in the ocean (Sclater et al., 1976).
387 Biological processes are generally accompanied by a kinetic isotope fractionation, where the lighter
388 isotope is preferentially concentrated in the biomass, forcing the residual reservoir towards a heavier
389 isotopic composition (e.g., Valley and Cole, 2001). However, almost constant TOC concentrations
390 and extremely low productivity contradict this scenario (Fig. 3F-H). In the latter regard, Mn×Co
391 values are commonly utilized to assess oceanic upwelling and hence supply of deep water nutrients,
392 as Mn and Co are significantly depleted in modern upwelling sediments, with an upper threshold of
393 0.4 (Sweere et al., 2016). Application of this proxy to our samples suggests a relatively low overall
394 level of upwelling, and, in particular, the high-δ^{60}Ni interval at 100-250 mbsf (Fig. 6B) coincided
395 with a pronounced upwelling minimum (Fig. 3H), implying low productivity in conjunction with
396 ^{60}Ni-enrichment. Moreover, most Ba concentration values (20 out of 22 samples) correlate well with
397 Al (Fig. S1; $r = +0.90$, $p < 0.01$, $n = 20$) and fall close to the detrital regression line (with a slope of

0.005), indicating that most samples contain little Ba_{bio}. Therefore, our data suggest low productivity resulting from weakened upwelling (Fig. 3G-H), and, consequently, Ni uptake by phytoplankton biomass being the main cause of ^{60}Ni-enrichment is unlikely.

The third potential explanation for high pyrite δ^{60}Ni values requires Rayleigh-type distillation in a closed porewater system. Assuming the initial porewater δ^{60}Ni is equivalent to that of seawater (i.e., +1.44‰; Cameron and Vance, 2014), and considering a constant fractionation factor during Ni-sulfide formation (i.e., –0.66‰; Fujii et al., 2014; Vance et al., 2016), independent of any other fractionation, a Rayleigh-type distillation for pyrite nickel isotopes is depicted in Figure 9A. If porewater Ni was depleted to a level where only ~5% remained, pyrite would yield a δ^{60}Ni value of +2.72‰. By the same reasoning, if porewater sulfate were consumed to a level where only 0.8% remained, pyrite would acquire a δ^{34}S signature of +142.8‰ (Fig. 9B). The elevated sedimentation rates during deposition would have facilitated the rapid establishment of a closed porewater system (Fig. 2), because higher sedimentation rates reduce the exchange of sulfate between sediment porewaters and the overlying water column (Liu et al., 2021). In addition, extremely low S/C ratios (0.26 ± 0.09, n = 13; Li et al., 2022) and relatively higher $\delta^{13}C_{TIC}$ values at this site (minimum –0.60‰, vs. minima of –8.60‰ and –4.58‰ at two other sites in the Shenhu area; Li et al., 2022) support the argument that there was insufficient porewater sulfate to extensively remineralize organic matter via OSR. Although our calculations may underestimate the depletion of Ni and sulfate due to the potential involvement of other fractionation processes (e.g., biomass uptake fractionating Ni isotopes, and elemental sulfur disproportionation affecting sulfur fractionations; Cameron et al., 2009; Fike et al., 2015), Rayleigh-type distillation provides a plausible explanation for the extremely high nickel and sulfur isotopes values.

Lastly, the $\delta^{60}Ni$ of ferromanganese crusts in the South China Sea is distinctly higher than that of average seawater (+1.84 to +2.27‰; Gall et al., 2013). Therefore, the release of isotopically heavy Ni from manganese may have contributed to high pyrite $\delta^{60}Ni$. Fe- and Mn-(oxyhydr)oxides preferentially absorb MREEs from seawater (Smrzka et al., 2020), thus MREE enrichment may reflect the release of MREE from Fe- and Mn-(oxyhydr)oxides in the Fe/Mn reduction zone (Zone II) (Chen et al., 2015; Smrzka et al., 2020). MREE enrichment is observed in all samples (Fig. 4), suggesting that Fe/Mn reduction may have prevailed at the study site. In addition, the specific trace elements commonly released from Fe- and Mn-(oxyhydr)oxides are also observed in the pyrite trace-element data (see Section 5.4). The evidence presented above indicates that the reduction of Fe- and Mn-(oxyhydr)oxides likely also contributed to high pyrite $\delta^{60}Ni$ values.

In summary, since there is no clear relationship between pyrite $\delta^{60}Ni$ values and pyrite $\delta^{34}S$ or Ni concentrations (Fig. 10A and B), and since the pyrite $\delta^{60}Ni$ values cannot be explained by AOM uptake (Chen et al., 2023) or mixing of two endmembers (Zhao et al., 2021), the Ni isotopic compositions were likely dominantly influenced by a combination of the release of isotopically heavy Ni from Fe- and Mn-(oxyhydr)oxides, and Rayleigh-type distillation in a closed porewater system. In addition, we note that Ni inputs from continental weathering and biomass uptake cannot be completely excluded, because the high-$\delta^{60}Ni$ interval corresponds to increased Al_2O_3 contents (Figs. 3B and 6B), while Ni uptake by biomass can facilitate Rayleigh-type distillation. On the other hand, under conditions of low porewater sulfate due to the closed porewater system, as evidenced by low S/C ratios and high $\delta^{13}C_{TIC}$, Rayleigh-type distillation during SD-AOM at a relatively late diagenetic stage is likely to have been responsible for the extremely high $\delta^{34}S$ values.

5.4. Pyrite trace elements linked to OSR, SD-AOM and Fe/Mn reduction by organic matter or methane

Many siderophile and chalcophile trace elements are concentrated in early-formed pyrite (Huerta-Diaz and Morse, 1992; Large et al., 2009), and previous studies have demonstrated that the trace-element content of pyrite is related to the elemental composition of the seawater or pore fluid from which it forms (Tribovillard et al., 2008; Pisarzowska et al., 2014; Large et al., 2014). Since both SD-AOM and OSR can generate H_2S, pyrite formation linked to these processes may yield characteristic trace-element patterns owing to the different microbial pathways employed and their association with specific trace nutrients or metalloenzymes (Smrzka et al., 2020). The OSR process can release organic-matter-related trace elements (e.g., Cu and Zn) to the porewater during the consumption of organic matter, and these trace elements can be taken up by subsequently formed pyrite (Chen et al., 2023). On the other hand, because Ni and Co are required for enzyme synthesis in reverse methanogenesis (i.e., SD-AOM) (Glass and Orphan, 2012), their concentrations in authigenic pyrite tend to be higher when SD-AOM processes are active (e.g., Lin et al., 2022; Chen et al., 2023). Microbial methanogenesis incorporates Ni into the methyl coenzyme M reductase enzyme (Mcr) (Scheller et al., 2010), and ANME (anaerobic methanotrophic archaea) anaerobically oxidizes methane by running the methanogenesis pathway in reverse, with an enzyme that is similar to Mcr (Hallam et al., 2003; Mayr et al., 2008). Under sulfidic conditions, nickel liberated from AOM-modified biomass is readily taken up as insoluble NiS in the lattice of authigenic pyrite (Huerta-Diaz and Morse, 1992; Gregory et al., 2014, 2022; Large et al., 2014). Moreover, nickel isotopes have been used to trace Mcr-related nickel uptake due to preferential utilization of isotopically light Ni with a fractionation down to –1.46‰ (Cameron et al., 2009; Gueguen et al., 2013; Zhao et al., 2021). This

fractionation has also been generated during the reverse methanogenesis via the SD-AOM process (Chen et al., 2023).

Because multiple factors likely contributed to pyrite δ^{60}Ni values at Site SC03 (see Section 5.3), Mcr-driven fractionation of Ni cannot specifically be identified. However, the trace-element contents of pyrite at Site SC03 still demonstrate patterns similar to that observed in the theoretical scenario, i.e., Co and Ni are relatively enriched in high-δ^{34}S, SD-AOM-dominated pyrite, whereas Cu and Zn are enriched in low-δ^{34}S, OSR-dominated pyrite (Fig. 7). In addition, pyrite trace elements can also distinguish Fe-Mn reduction pathways (i.e., by dissimilatory Fe reduction or by methane). The dissolution of Fe/Mn-(oxyhydr)oxides occurs via:

$$4FeOOH + CH_2O + 7H^+ \rightarrow 4Fe^{2+} + HCO_3^- + 6H_2O \quad (5)$$

$$4MnOOH + CH_2O + 7H^+ \rightarrow 4Mn^{2+} + HCO_3^- + 6H_2O \quad (6)$$

These reactions will release trace elements captured by Fe/Mn-(oxyhydr)oxides (e.g., As) as well as by organic matter (e.g., Cu and Zn). This situation is complicated by the abiotic reductive dissolution of Fe/Mn-(oxyhydr)oxides by dissolved sulfide. However, since reaction rates are most rapid in the zone where the most reactive Fe-(oxyhydr)oxide minerals persist (dominantly Zones II-III; Canfield, 1989), it might be expected that this process will dominantly result in pyrite that has a trace element composition similar to that produced by OSR, although this process may also capture a signal from SD-AOM.

When upwelling methane comes into contact with sedimentary Fe/Mn-(oxyhydr)oxides, the following reactions can occur (Beal et al., 2009):

$$CH_4 + 8Fe(OH)_3 + 15H^+ \rightarrow HCO_3^- + 8Fe^{2+} + 21H_2O \quad (7)$$

$$CH_4 + 4MnO_2 + 7H^+ \rightarrow HCO_3^- + 4Mn^{2+} + 5H_2O \quad (8)$$

These reactions can liberate trace elements from particulate Fe/Mn-(oxyhydr)oxides, as in the Fe/Mn-AOM zone (Zone V) of Site SC03. On the other hand, the Fe/Mn-AOM process does not liberate trace elements from organic matter. This difference allows us to distinguish different Fe/Mn reduction pathways.

To make use of this distinction, we consider pyrite As content relative to specific trace-element concentrations. Iron-(oxyhydr)oxides are the most important carrier phases of As, which is adsorbed from the water column and ultimately released to sediment porewaters under reducing conditions (Andreae, 1979; Sullivan and Aller, 1996). Both arsenate and arsenite have a high sorption affinity for manganese and iron (oxyhydr)oxides (Pierce and Moore, 1982; Peterson and Carpenter, 1986), and arsenic is cycled near or at the zone of Fe/Mn reduction (Widerlund and Ingri, 1995; Chaillou et al., 2003). Iron sulfide minerals such as pyrite and arsenopyrite (FeAsS) are considered the most effective long-term sinks for As in sulfidic sediments (Morse and Luther, 1999). Thus, pyrite As concentrations can help to identify the dissolution of Fe/Mn-(oxyhydr)oxides. The SD-AOM-dominated, high-δ^{34}S pyrites (Fig 10C-D, pink arrows and orange squares) show a sharp increase in As content but little to no change in Cu or Zn, the latter being associated mainly with the organic fraction of the sediment, suggesting that Fe/Mn-AOM may have occurred near the SD-AOM zone, such that high-δ^{34}S pyrite captured porewater As released from dissolving Fe/Mn-(oxyhydr)oxides. On the other hand, most OSR-dominated, low-δ^{34}S pyrites (Fig 10C-D, blue arrows and green circles) show synchronous increases in As as well as Cu and Zn, implying release of the latter due to organic matter oxidation concurrently with release of the former due to reduction of Fe/Mn-(oxyhydr)oxides. Furthermore, most of the SD-AOM-dominated, high-δ^{34}S pyrites show synchronous increases in As as well as Co and Ni (Fig. 10E-F, pink arrows and orange squares), implying SD-AOM-associated

pyrite captured both Mcr-released Co and Ni, and As released via Fe/Mn-AOM. However, there is little or no relationship to OSR-dominated, low-$\delta^{34}S$ pyrite (Fig. 10E-F, green circles) because Co and Ni also form strong complexes with organic matter (Smrzka et al., 2019). When Fe/Mn-(oxyhydr)oxides are reduced during organic matter oxidation, Ni and Co may be released to porewaters and subsequently taken up by authigenic pyrite. Fe/Mn-AOM (Zone V) can occur at any depth below the Fe/Mn reduction zone (Zone II) depending on the methane flux and the Fe- and Mn-(oxyhydr)oxides remaining. Indeed, some samples give a potential composite signal resulting from the interplay between the two Fe/Mn reduction pathways (Fig. 10E and F).

In summary, based on differences in the timing of trace-element liberation and uptake in pyrite, the pathways of pyrite formation and trace-element cycling linked to Fe/Mn reduction, OSR, SD-AOM and Fe/Mn-AOM can be traced (Fig. 11). We infer that Cu and Zn were released from organic matter through Fe/Mn reduction and OSR (Zones II and III), whereas As was released from Fe/Mn-(oxyhydr)oxides. Therefore, OSR-dominated pyrite has low $\delta^{34}S$ and is enriched in As, Cu and Zn (green circles in Figs. 6, 7, 10 and 11). During SD-AOM in Zone IV, organic decomposition linked to Mcr released Ni and Co to porewaters, promoting their incorporation into SD-AOM-associated pyrite. If Fe/Mn-AOM also prevails in this zone, As released from Fe/Mn-(oxyhydr)oxides is incorporated into SD-AOM-related pyrite (orange squares in Figs. 6, 7, 10 and 11). As abiotic Fe reduction can occur in Zones II-IV, depending on the availability of dissolved sulfide from OSR or SD-AOM, it is challenging to differentiate pyrite formed during this process based solely on trace element analyses.

6. Conclusions

We have investigated the $\delta^{34}S$, $\delta^{60}Ni$ and trace element composition of authigenic pyrite aggregates, as well as major- and trace- element compositions of bulk sediment, from the mid-Pliocene of the Shenhu area, PRMB, South China Sea (Site GMGS4-SC-03). Pyrite formed in conjunction with SD-AOM has high $\delta^{34}S$ values (up to 142.8‰) and contain wider framboidal overgrowths. Pyrite $\delta^{60}Ni$ values show no relationship with pyrite formation pathways, but extremely high pyrite $\delta^{60}Ni$ values (up to 2.72‰) were dominated by the release of isotopically heavy Ni from Fe/Mn-(oxyhydr)oxides, accompanied by Rayleigh-type distillation in a closed porewater system. In terms of trace element patterns in pyrite, SD-AOM-associated pyrite is enriched in Co and Ni due to uptake by reverse methanogenesis and subsequent incorporation into the pyrite structure. By contrast, OSR-associated pyrite is enriched in Cu and Zn due to OSR-related release of trace elements from decaying organic matter. In addition, the relationships between both As and Cu and/or Zn, and As and Co and/or Ni, has the potential to distinguish Fe/Mn-(oxyhydr)oxides reduced by organic matter and methane, respectively. Thus, our results are significant in demonstrating the potential utility of pyrite trace element compositions to distinguish Fe/Mn reduction, OSR, SD-AOM and Fe/Mn-AOM.

Acknowledgments

This research was supported by the National Natural Science Foundation of China (Grant Nos. 42302215 and 42276068), and Open Funds for Hubei Key Laboratory of Marine Geological Resources (MGR202304). We would like to thank Liyuan Xu for sulfur isotopic analysis and pyrite SEM images. We are also grateful to the editor Christian France-Lanord, reviewer Bleuenn Guéguen and another anonymous reviewer for their constructive comments.

552

553 **Appendix A. Supplementary materials**

554 The supplementary materials include a crossplot of Ba vs Al (Figure S1), variations of
555 MREE/MREE* and Eu/Eu* (Figure S2), crossplots of MREE/MREE* and Eu/Eu* vs Al_2O_3 (wt%)
556 (Figure S3), crossplots of pyrite geochemistry versus bulk-rock geochemistry (Figure S4),
557 uncertainties of elemental concentrations in pyrite extracts (Table S1), and pyrite framboidal
558 overgrowth widths and nucleus diameters (Table S4). The supplementary materials also include other
559 research data: i.e., major element oxide contents of bulk sediments (Table S2) and trace elements and
560 rare earth elements, along with their corresponding calculations (Table S3).

561

562 **References**

563 Andreae, M.O., 1979. Arsenic speciation in seawater and interstitial waters: the influence of
564 biological-chemical interactions on the chemistry of a trace element. Limnol Oceanogr 24, 440–
565 452

566 Beal, E.J., House, C.H., Orphan, V.J., 2009. Mn Fe Dependent Marine Methane Oxidation. Science
567 325, 184–187.

568 Berner, R. A., 2002. Examination of hypotheses for the Permo-Triassic boundary extinction by carbon
569 cycle modeling. Proc. Natl Acad. Sci. USA 99, 4172–4177.

570 Bonn, W.J., Gingele, F.X., Grobe, H., Mackensen, A., Fütterer, D.K., 1998. Palaeoproductivity at the
571 Antarctic continental margin: opal and barium records for the last 400 ka. Palaeogeogr.
572 Palaeoclimatol. Palaeoecol. 139 (3), 195–211.

573 Borowski, W.S., 2004. A review of methane and gas hydrate in the dynamic, stratified system of the
574 Black Ridge region, offshore southeastern North America. Chemical Geology 205, 311–346.

575 Borowski, W.S., Rodriguez, N.M., Paull, C.K., Ussler III, W., 2013. Are ^{34}S-enriched authigenic
576 sulfide minerals a proxy for elevated methane flux and gas hydrates in the geologic record?
577 Marine and Petroleum Geology, 43, 381–395.

578 Butler, I.B., Rickard, D., 2000. Framboidal pyrite formation via the oxidation of iron, II. monosulfide
579 by hydrogen sulphide. Geochim. Cosmochim. Acta 64, 2665–2672
580 Canfield, D.E., 1989. Reactive iron in marine sediments. Geochim. Cosmochim. Acta 53, 619-632.
581 Canfield, D.E., 2001. Isotope fractionation by natural populations of sulfate-reducing bacteria.
582 Geochim. Cosmochim. Acta 65, 1117–1124.
583 Canfield, D.E., Thamdrup, B., 2009. Towards a consistent classification scheme for geochemical
584 environments, or, why we wish the term 'suboxic' would go away. Geobiology 7, 385-392.
585 Cameron, V., Vance, D., Archer, C., House, C.H., 2009. A biomarker based on the stable isotopes of
586 nickel. Proceedings of the National Academy of Sciences of the United States of America 106,
587 10944-10948.
588 Cameron, V., Vance, D., 2014. Heavy nickel isotope compositions in rivers and the oceans.
589 Geochimica et Cosmochimica Acta 128, 195-211.
590 Chaillou, G., Schäfer, J., Anschutz, P., Lavaux, G., Blanc, G., 2003. The behaviour of arsenic in
591 muddy sediments of The Bay of Biscay (France). Geochim. Cosmochim. Acta 67, 2993–3003
592 Chen, C., Wang, J., Algeo, T.J., Zhu, J.-M., Wang, Z., Ma, X., Cen, Y., 2023. Sulfate-driven anaerobic
593 oxidation of methane inferred from trace-element chemistry and nickel isotopes of pyrite.
594 Geochimica et Cosmochimica Acta 349, 81–95.
595 Chen, F., Su, X., Zhou, Y., 2013. Late Miocene-Pleistocene calcareous nannofossil biostratigraphy of
596 Shenhu gas hydrate drilling area in the South China Sea and variations in sedimentation rates.
597 Earth Science-Journal of China University of Geosciences 38(1), 1–9, doi:
598 10.3799/dqkx.2013.001 (in Chinese with English abstract).
599 Cheng, C., Jiang, T., Kuang, Z., Yang, C., Zhang, C., He, Y., Cheng, Z., Tian, D., Xiong, P., 2020.
600 Characteristics of gas chimneys and their implications on gas hydrate accumulation in the
601 Shenhu area, northern south China sea. Journal of Natural Gas Science and Engineering 84,
602 103629.
603 Chen, J., Algeo, T.J., Zhao, L., Chen, Z.-Q., Cao, L., Zhang, L., Li, Y., 2015. Diagenetic uptake of
604 rare earth elements by bioapatite, with an example from Lower Triassic conodonts of South
605 China. Earth-Science Reviews 149, 181-202.
606 Claypool, G.E., Kaplan, I.R., 1974. The origin and distribution of methane in marine sediments.
607 Kaplan, I.R., ed., Natural Gases in Marine Sediments. Plenum Press, New York, 99–139.

608 Dymond, J., Suess, E., Lyle, M., 1992. Barium in deep-sea sediment: a geochemical proxy for
609 paleoproductivity. Paleoceanography 7 (2), 163–181.
610 Feng, D., Qiu, J.-W., Hu, Y., Peckmann, J., Guan, H., Tong, H., Chen, C., Chen, J., Gong, S., Li, N.,
611 Chen, D., 2018. Cold seep systems in the South China Sea: An overview. J. Asian Earth Sci. 168,
612 3–16.
613 Fike, D.A., Bradley, A.S., Rose, C.V., 2015. Rethinking the ancient sulfur cycle. Annu. Rev. Earth
614 Planet. Sci. 43 (1), 593–622
615 Fujii, T., Moynier, F., Blichert-Toft, J., Albarède, F., 2014. Density functional theory estimation of
616 isotope fractionation of Fe, Ni, Cu, and Zn among species relevant to geochemical and biological
617 environments. Geochim. Cosmochim. Acta 140, 553–576.
618 Gall, L., Williams, H.M., Siebert, C., Halliday, A.N., Herrington, R.J., Hein, J.R., 2013. Nickel
619 isotopic compositions of ferromanganese crusts and the constancy of deep ocean inputs and
620 continental weathering effects over the Cenozoic. Earth and Planetary Science Letters 375, 148–
621 155.
622 Glass, J.B., Orphan, V.J., 2012. Trace metal requirements for microbial enzymes involved in the
623 production and consumption of methane and nitrous oxide. Front. Microbiol. 3 (61), 1–20.
624 Gong, C.L., Wang, Y.M., Zhu, W.L., Li, W.G., Xu, Q., 2013. Upper Miocene to Quaternary
625 unidirectionally migrating deep-water channels in the Pearl River Mouth Basin, northern South
626 China Sea. Aapg. Bull. 97, 285–308.
627 Gregory, D.D., Meffre, S., Large, R.R., 2014. Comparison of metal enrichment in pyrite framboids
628 from a metal-enriched and metal-poor estuary. Am. Mineral. 99, 633–644.
629 Gregory, D.D., Kovarik, L., Taylor, S.D., Perea, D.E., Owens, J.D., Atienza, N., Lyons, T. W., 2022.
630 Nanoscale trace-element zoning in pyrite framboids and implications for paleoproxy
631 applications. Geology 50 (6), 736–740.
632 Gueguen, B., Rouxel, O., Ponzevera, E., Bekker, A., Fouquet, Y., 2013. Nickel isotope variations in
633 terrestrial silicate rocks and geological reference materials measured by MC-ICP-MS. Geostand.
634 Geoanal. Res. 37 (3), 297–317.
635 Hallam, S.J., Girguis, P.R., Preston, C.M., Richardson, P.M., Delong, E.F., 2003. Identification of
636 methyl coenzymeMreductase A (mcrA) genes associated with methane-oxidizing archaea. Appl.
637 Environ. Microbiol. 69, 5483–5491.

He, Y., Xie, X., Kneller, B.C., Wang, Z., Li, X., 2013. Architecture and controlling factors of canyon fills on the shelf margin in the Qiongdongnan Basin, northern South China Sea. Mar. Petrol. Geol. 41, 264–276.

He, M., Zhong, G., Liu, X., Liu, L., Shen, X., Wu, Z., Huang, K., 2017. Rapid post-rift tectonic subsidence events in the Pearl River Mouth Basin, northern South China sea margin. J. Asian Earth Sci. 147, 271–283.

He, Y., Kuang, Z., Cheng, C., Jiang, T., Zhang, C., Lu, B., Yang, C., Liu, J., Xiang, C., 2022. Effects of Depositional Processes in Submarine Canyons and Distribution of Gas Chimneys on Gas Hydrate Accumulation in the Shenhu Sea Area, Northern South China Sea. Energies 16, 234.

Hesselbo, S.P., Grocke, D.R., Jenkyns, H.C., Bjerrum, C.J., Farrimond, P., Bell, H.S.M., Green, O.R., 2000. Massive dissociation of gas hydrate during a Jurassic oceanic anoxic event. Nature 406, 392–395.

Huerta-Diaz, M.A., Morse, J.W., 1992. Pyritisation of trace elements metals in anoxic marine sediments. Geochim. Cosmochim. Acta 56, 2681–2702.

Jiang, G.Q., Kennedy, M.J., Christie-Blick, N., 2003. Stable isotopic evidence for methane seeps in Neoproterozoic postglacial cap carbonates. Nature 426, 822– 825.

Jørgensen, B.B., Böttcher, M.E., Lüschen, H., Neretin, L.N., Volkov, I.I., 2004. Anaerobic methane oxidation and a deep H_2S sink generate isotopically heavy sulfides in Black Sea sediments. Geochimica et Cosmochimica Acta, 68(9): 2095–2118.

Jørgensen, B.B., Kasten, S., 2006. Sulfur cycling and methane oxidation. In: Schulz, H.D., Zabel, M., ed. Marine geochemistry. Berlin: Springer, 271–310.

Kong, L., Chen, H., Ping, H., Zhai, P., Liu, Y., Zhu, J., 2018. Formation pressure modeling in the Baiyun Sag, northern South China Sea: implications for petroleum exploration in deep-water areas. Mar. Petrol. Geol. 97, 154–168.

Krom, M.D., Mortimer, R.J.G., Poulton, S., Hayes, P., Davies, I.M., Davison, W., Zhang, H., 2002. In-situ determination of dissolved iron production in recent marine sediments. Aquatic Sciences 64, 282-291.

Lachance, G.R., Claisse, F., 1995. Quantitative X-ray Fluorescence Analysis Theory and Application. John Wiley & Sons, New York

Large, R.R., Halpin, J.A., Danyushevsky, L.V., Maslennikov, V.V., Bull, S.W., Long, J.A., Gregory,

668 D.D., Lounejeva, E., Lyons, T.W., Sack, P.J., McGoldrick, P.J., Calver, C.R., 2014. Trace element
669 content of sedimentary pyrite as a new proxy for deep-time ocean–atmosphere evolution. Earth
670 Planet. Sci. Lett. 389, 209–220.
671 Large, R.R., Danyushevsky, L., Hollit, C., Maslennikov, V., Meffre, S., Gilbert, S., Bull, S., Scott, R.,
672 Emsbo, P., Thomas, H., Singh, B., Foster, J., 2009. Gold and trace element zonation in pyrite
673 using a laser imaging technique: Implications for the timing of gold in orogenic and carlin-style
674 sediment-hosted deposits. Econ. Geol. 104, 635–668.
675 Lawrence, M.G., Greig, A., Collerson, K.D., Kamber, B.S., 2006. Rare Earth Element and Yttrium
676 Variability in South East Queensland Waterways. Aquat. Geochem. 12, 39-72.
677 Li, Y., Xu, X., Pang, L., Guan, P., Fang, Y., Lu, H., Ye, J., Xie, W., 2022. Elemental and Isotopic
678 Signatures of Bulk Sedimentary Organic Matter in Shenhu Area, Northern South China Sea.
679 Frontiers in Earth Science 10, doi: 10.3389/feart.2022.836381
680 Libes, S.M., 2009. Introduction to Marine Biogeochemistry. 2nd ed. Burlington-San Diego-London:
681 Elsevier Academic Press. 169–324
682 Lin, Q., Wang, J., Algeo, T.J., Sun, F., Lin, R., 2016. Enhanced framboidal pyrite formation related
683 to anaerobic oxidation of methane in the sulfate-methane transition zone of the northern South
684 China Sea. Mar. Geol. 379, 100–108.
685 Lin, Z., Sun, X., Peckmann, J., Lu, Y., Xu, L., Strauss, H., Zhou, H., Gong, J., Lu, H., Teichert, B.M.A.,
686 2016. How sulfate-driven anaerobic oxidation of methane affects the sulfur isotopic composition
687 of pyrite: A SIMS study from the South China Sea. Chemical Geology 440, 26–41.
688 Lin, Z., Sun, X., Strauss, H., Lu, Y., Gong, J., Xu, L., Lu, H., Teichert, B.M.A., Peckmann, J., 2017.
689 Multiple sulfur isotope constraints on sulfate-driven anaerobic oxidation of methane: Evidence
690 from authigenic pyrite in seepage areas of the South China Sea. Geochimica et Cosmochimica
691 Acta 211, 153-173.
692 Lin, Z., Sun, X., Chen, K., Strauss, H., Klemd, R., Smrzka, D., Chen, T., Lu, Y., Peckmann, J., 2022.
693 Effects of sulfate reduction processes on the trace element geochemistry of sedimentary pyrite
694 in modern seep environments. Geochim. Cosmochim. Acta 333, 75–94.
695 Liu, J., Izon, G., Wang, J., Antler, G., Wang, Z., Zhao, J., Egger, M., 2018. Vivianite formation in
696 methane-rich deep-sea sediments from the South China Sea. Biogeosciences 15, 6329-6348.
697 Liu, J., Pellerin, A., Izon, G., Wang, J., Antler, G., Liang, J., Su, P., Jørgensen, B.B., Ono, S., 2020.

698 The multiple sulphur isotope fingerprint of a sub-seafloor oxidative sulphur cycle driven by iron.
699 Earth and Planetary Science Letters 536, 116165.
700 Liu, J., Antler, G., Pellerin, A., Izon, G., Dohrmann, I., Findlay, A.J., Røy, H., Ono, S., Turchyn, A.V.,
701 Kasten, S., Jørgensen, B.B., 2021. Isotopically "heavy" pyrite in marine sediments due to high
702 sedimentation rates and non-steady-state deposition. Geology 49 (7), 816–821.
703 Liu, J., Pellerin, A., Wang, J., Rickard, D., Antler, G., Zhao, J., Wang, Z., Jørgensen, B.B., Ono, S.,
704 2022. Multiple sulfur isotopes discriminate organoclastic and methane-based sulfate reduction
705 by sub-seafloor pyrite formation. Geochimica et Cosmochimica Acta 316, 309-330.
706 Mayr, S., Latkoczy, C., Krüger, M., Günther, D., Shima, S., Thauer, R.K., Widdel, F., Jaun, B., 2008.
707 Structure of an F430 variant from archaea associated with anaerobic oxidation of methane. J.
708 Am. Chem. Soc. 130, 10758–10767.
709 Mi, L., Zhang, Z., Pang, X., Liu, J., Zhang, B., Zhao, Q., Feng, X., 2018. Main controlling factors of
710 hydrocarbon accumulation in Baiyun Sag at northern continental margin of South China Sea.
711 Pet. Explor. Dev. 45, 963–973
712 Morse, J.W., Luther, G.W., 1999. Chemical influences on trace metal-sulfde interactions in anoxic
713 sediments. Geochim. Cosmochim. Acta 63, 3373–3378
714 Neretin, L.V., Böttcher, M.E., Jørgensen, B.B., 2004. Pyritization processes and greigite formation in
715 the advancing sulfidization front in the Upper Pleistocene sediments of the Black Sea. Geochim.
716 Cosmochim. Acta 68, 2081–2093.
717 Ohfuji, H., Rickard, D., 2005. Experimental syntheses of framboids-a review. Earth-Sci. Rev. 71,
718 147–170.
719 Ono, S., Wing, B., Johnston, D., Farquhar, J., Rumble, D., 2006. Mass-dependent fractionation of
720 quadruple stable sulfur isotope system as a new tracer of sulfur biogeochemical cycles. Geochim.
721 Cosmochim. Acta 70, 2238–2252.
722 Paradis, S., Puig, P., Sanchez-Vidal, A., Masqué, P., Garcia-Orellana, J., Calafat, A., Canals, M., 2018.
723 Spatial distribution of sedimentation-rate increases in Blanes Canyon caused by technification
724 of bottom trawling fleet. Progress in Oceanography 169, 241–252.
725 Pasquier, V., Sansjofre, P., Rabineau, M., Revillon, S., Houghton, J., Fike, D.A., 2017. Pyrite sulfur
726 isotopes reveal glacial-interglacial environmental changes. Proc. Natl. Acad. Sci. U.S.A. 114
727 (23), 5941–5945.

728 Peterson, M.L., Carpenter, R., 1986. Arsenic distributions in porewaters and sediments of Puget
729 Sound, Lake Washington, the Washington coast and Saanich Inlet, B.C. Geochim. Cosmochim.
730 Acta 50, 353–369
731 Peketi, A., Joshi, R.K., Patil, D.J., Srinivas, P.L., Dayal, A.M., 2012. Tracing the Paleo sulfate-
732 methane transition zones and H2S seepage events in marine sediments: An application of C-S-
733 Mo systematics. Geochemistry, Geophysics, Geosystems, 13(10), doi: 10.1029/2012/GC004288.
734 Pierce, M.L., Moore, C.B., 1982. Adsorption of arsenite and arsenate on amorphous iron hydroxide.
735 Water Res. 16, 1247–1253
736 Pisarzowska, A., Berner, Z.A., Racki, G., 2014. Geochemistry of Early Frasnian (Late Devonian)
737 pyrite-ammonoid level in the Kostomłoty Basin, Poland, and a new proxy parameter for
738 assessing the relative amount of syngenetic and diagenetic pyrite. Sediment. Geol. 308, 18–31.
739 Poulton, S.W., Krom, M.D., Raiswell, R., 2004. A revised scheme for the reactivity of iron
740 (oxyhydr)oxide minerals towards dissolved sulfide. Geochimica et Cosmochimica Acta 68,
741 3703-3715.
742 Prakash Babu, C., Brumsack, H.-J., Schnetger, B., Böttcher, M.E., 2002. Barium as a productivity
743 proxy in continental margin sediments: a study from the eastern Arabian Sea. Mar. Geol. 184,
744 189–206.
745 Reitz, A., Pfeifer, K., de Lange, G.J., Klump, J., 2004. Biogenic barium and the detrital Ba/Al ratio:
746 a comparison of their direct and indirect determination. Mar. Geol. 204, 289–300
747 Ren, J., Cheng, C., Jiang, T., Kuang, Z., Lai, H., Liang, J., Chen, Z., Li, T., 2023. Faults and gas
748 chimneys jointly dominate the gas hydrate accumulation in the Shenhu Area, northern South
749 China Sea. Frontiers in Marine Science 10, 1254410.
750 Rickard, D., Luther, G.W.I.I.I., 2007. Chemistry of iron sulfides. Chem. Rev. 107, 514–562
751 Rutsch, H.-J., Mangini, A., Bonani, G., Dittrich-Hannen, B., Kubik, P.W., Suter, M., Segl, M., 1995.
752 ^{10}Be and Ba concentrations in West African sediments trace productivity in the past. Earth Planet.
753 Sci. Lett. 133, 129–143.
754 Scheller, S., Goenrich, M., Boecher, R., Thauer, R.K., Jaun, B., 2010. The key nickel enzyme of
755 methanogenesis catalyses the anaerobic oxidation of methane. Nature 465 (7298), 606–608.
756 Schoepfer, S.D., Shen, J., Wei, H., Tyson, R.V., Ingall, E., Algeo, T.J., 2015. Total organic carbon,
757 organic phosphorus, and biogenic barium fluxes as proxies for paleomarine productivity. Earth-

758 Sci. Rev. 149, 23–52.
759 Sclater, F., Boyle, E., Edmond, J., 1976. On the marine geochemistry of nickel. Earth Planet. Sci. Lett.
760 31, 119–128.
761 Shen, J., Schoepfer, S.D., Feng, Q., Zhou, L., Yu, J., Song, H., Wei, H., Algeo, T.J., 2015. Marine
762 productivity changes during the end-Permian crisis and Early Triassic recovery. Earth-Science
763 Reviews 149, 136-162.
764 Smrzka, D., Zwicker, J., Bach, W., Feng, D., Himmler, T., Chen, D., Peckmann, J., 2019. The behavior
765 of trace elements in seawater, sedimentary pore water, and their incorporation into carbonate
766 minerals: a review. Facies 65, doi: 10.1007/s10347-019-0581-4
767 Smrzka, D., Feng, D., Himmler, T., Zwicker, J., Hu, Y., Monien, P., Tribovillard, N., Chen, D.,
768 Peckmann, J., 2020. Trace elements in methane-seep carbonates: Potentials, limitations, and
769 perspectives. Earth-Science Reviews 208, 103263.
770 Spivak-Birndorf, L.J., Wang, S.-J., Bish, D.L., Wasylenki, L.E., 2018. Nickel isotope fractionation
771 during continental weathering. Chemical Geology 476, 316-326.
772 Su, Z., Cao, Y., Wu, N., Chen, D., Yang, S., Wang, H., 2012. Numerical investigation on methane
773 hydrate accumulation in Shenhu Area, northern continental slope of South China Sea. Marine
774 and Petroleum Geology 38, 158–165.
775 Sullivan, K.A., Aller, R.C., 1996. Diagenetic cycling of arsenic in Amazon shelf sediments. Geochim.
776 Cosmochim. Acta 60, 1465–1477
777 Sun, Q., Wu, S., Cartwright, J., Dong, D., 2012. Shallow gas and focused fluid flow systems in the
778 Pearl River Mouth Basin, northern South China Sea. Mar. Geol. 315, 1–14.
779 Sun, Q., Cartwright, J., Xie, X., Lu, X., Yuan, S., Chen, C., 2018. Reconstruction of repeated
780 Quaternary slope failures in the northern South China Sea. Marine Geology 401, 17–35.
781 Sweere, T., Boorn, S., Dickson, A.J., Reichart, G., 2016. Definition of new trace-metal proxies for
782 the controls on organic matter enrichment in marine sediments based on Mn, Co, Mo and Cd
783 concentrations. Chem. Geol. 441, 235–245
784 Taylor, K.G., Macquaker, J.H.S., 2011. Iron minerals in marine sediments record chemical
785 environments. Electrophoresis 7, 113–118
786 Taylor, S.R., McLennan, S.M., 1985. The Continental Crust: Its Composition and Evolution.
787 Blackwell, Oxford (312 pp)

788 Tian, J., Zhao, Q., Wang, P., Li, Q., Cheng, X., 2008. Astronomically modulated Neogene sediment
789 records from the South China Sea. Paleoceanography 23, doi: 10.1029/2007PA001552
790 Tribovillard, N., Lyons, T.W., Riboulleau, A., Bout-Roumazeilles, V., 2008. A possible capture of
791 molybdenum during early diagenesis of dysoxic sediments. Bull. Soc. Geol. Fr. 179, 3–12.
792 Valley, J., Cole, D., 2001. Reviews in Mineralogy & Geochemistry: Stable Isotope Geochemistry, vol.
793 43. Mineralogical Society of America.
794 Vance, D., Little, S.H., Archer, C., Cameron, V., Andersen, M.B., Rijkenberg, M.J., Lyons, T.W., 2016.
795 The oceanic budgets of nickel and zinc isotopes: the importance of sulfidic environments as
796 illustrated by the Black Sea. Phil. Trans. R. Soc. A 374, 20150294, doi: 10.1098/rsta.2015.0294
797 Wang, J., Jiang, G., Xiao, S., Li, Q., Wei, Q., 2008. Carbon isotope evidence for widespread methane
798 seeps in the ca. 635 Ma Doushantuo cap carbonate in south China. Geology 36 (5), 347–350.
799 Wang, D., Wu, S., Qin, Z., Ding, W., Cao, Q., 2009. Architecture and identification of large
800 Quaternary mass transport depositions in the slope of South China Sea (in Chinese with English
801 abstract). Mar. Geol. Quat. Geol. 5, 65–72.
802 Widerlund, A., Ingri, J., 1995. Early diagenesis of arsenic in sediments of the Kalix River estuary,
803 northern Sweden. Chem. Geol. 125, 185–196
804 Wilkin, R.T., Barnes, H.L., 1996. Pyrite formation by reactions of iron monosulfides with dissolved
805 inorganic and organic sulfur species. Geochim. Cosmochim. Acta 60, 4167–4179.
806 Wu, G., Zhu, J.M., Wang, X., Han, G., Tan, D., Wang, S.J., 2019. A novel purification method for
807 high precision measurement of Ni isotopes by double spike MC-ICP-MS. J. Anal. At. Spectrom.
808 34 (8), 1639–1651.
809 Wu, G., Zhu, J.M., Wang, X., Johnson, T.M., Han, G., 2020. High-Sensitivity Measurement of Cr
810 Isotopes by Double Spike MC-ICP-MS at the 10 ng Level. Analytical chemistry 92, 1463-1469.
811 Wu, G., Zhu, J.-M., Wang, X., Johnson, T.M., He, Y., Huang, F., Wang, L.-X., Lai, S.-C., 2022. Nickel
812 isotopic composition of the upper continental crust. Geochimica et Cosmochimica Acta 332,
813 263-284.
814 Xie, R., Wu, D., Liu, J., Sun, T., Liu, L., Wu, N., 2019. Geochemical Evidence of Metal-Driven
815 Anaerobic Oxidation of Methane in the Shenhu Area, the South China Sea. International journal
816 of environmental research and public health 16, doi: 10.3390/ijerph16193559
817 Yang, S., Lei, Y., Liang, J., Holland, M., Schultheiss, P., Lu, J., Wei, J., 2017. Concentrated Gas

Hydrate in the Shenhu Area, South China Sea: Results From Drilling Expeditions GMGS3 & GMGS4. Proceedings of 9th International Conference on Gas Hydrates, Denver 105, 1-16.

Yu, X., Liang, J., Fang, J., Cong, X., Jiang, L., Wang, J., 2012. Tectonic subsidence characteristics and its relationship to BSR distribution in deep water area of Pearl River Mouth Basin since the Late Miocene. Journal of Palaeogeography 14(6), 787–800 (in Chinese with English abstract).

Yu, X., Wang, J., Liang, J., Li, S., Zeng, X., Li, W., 2014. Depositional characteristics and accumulation model of gas hydrates in northern South China Sea. Marine and Petroleum Geology 56, 74-86.

Zhang, W., Liang, J., Wei, J., Lu, J.a., Su, P., Lin, L., Huang, W., Guo, Y., Deng, W., Yang, X., Wan, Z., 2020. Geological and geophysical features of and controls on occurrence and accumulation of gas hydrates in the first offshore gas-hydrate production test region in the Shenhu area, Northern South China Sea. Marine and Petroleum Geology 114, 104191.

Zhao, Z., Shen, B., Zhu, J.M., Lang, X., Wu, G., Tan, D., Pei, H., Huang, T., Ning, M., Ma, H., 2021. Active methanogenesis during the melting of Marinoan snowball Earth. Nature communications 12, 955, doi: 10.1038/s41467-021-21114-6

Zhu, M., Graham, S., Pang, X., McHargue, T., 2010. Characteristics of migrating submarine canyons from the middle Miocene to present: Implications for paleoceanographic circulation, northern South China Sea. Mar. Petrol. Geol. 27, 307–31

Figure captions

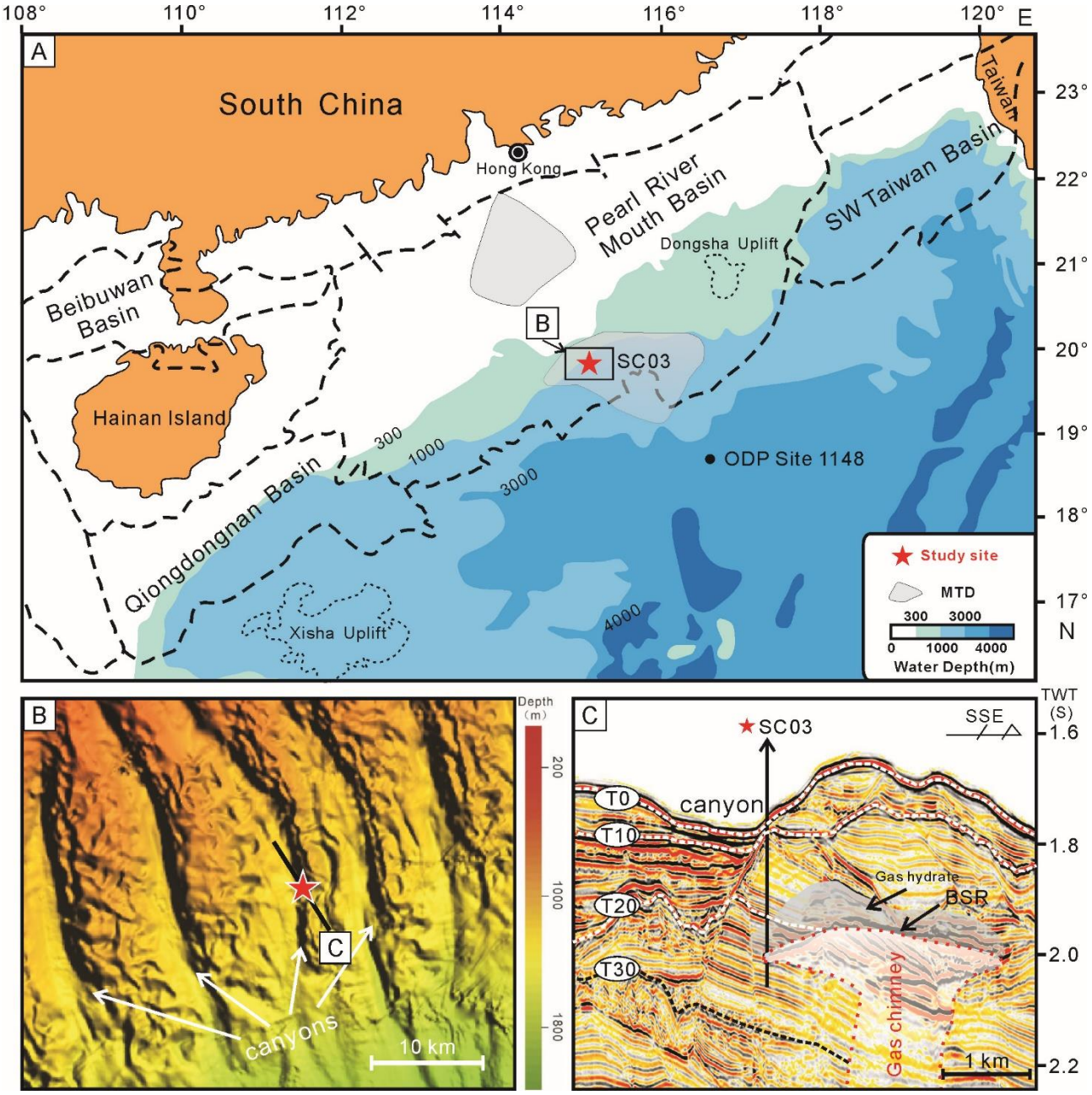

Fig. 1. (A) Location of Site SC03 (red star) in the Pearl River Mouth Basin (PRMB). Gray areas are affected by mass transport deposits (MTD). The black rectangle represents panel B. Modified from Wang et al. (2009) and Sun et al. (2012); (B) Multi-beam map of the seafloor showing several submarine canyons in the study area. The black line represents the seismic profile in panel C. Modified from He et al. (2022); (C) Seismic profile around Site SC03. The bottom-simulating reflector and inferred gas hydrate zone are from Zhang et al. (2020). The gas chimney (red dashed line) and the seismic horizons (dashed lines T0–T30) are from Cheng et al. (2020). TWT = two-way travel time.

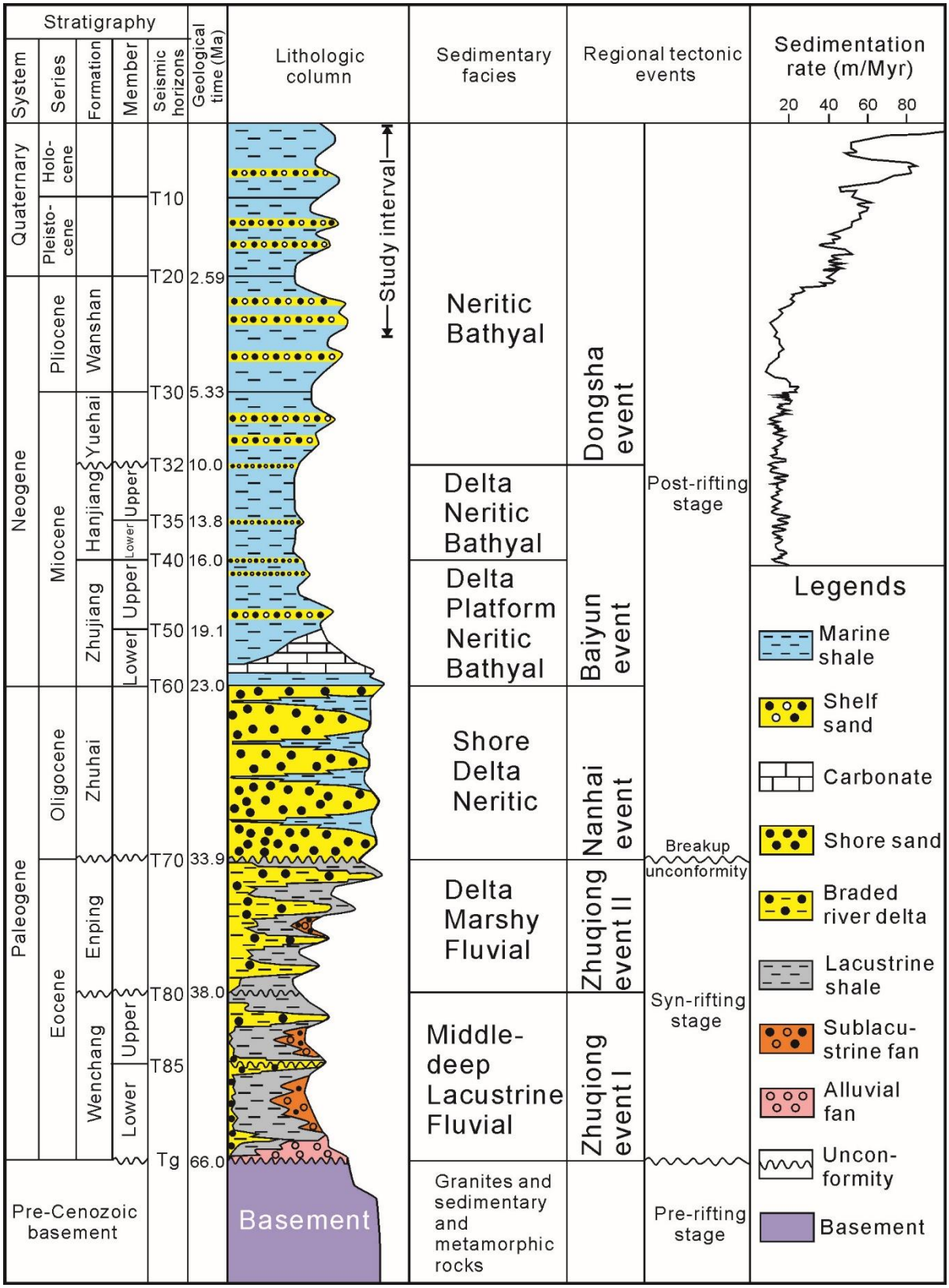

Fig. 2. Simplified chronological and stratigraphic profiles, in addition to tectonic events, in the PRMB (modified from Kong et al., 2018; Cheng et al., 2020). Sedimentation rates are from ODP Site 1148 (see Figure 1A; Tian et al., 2008).

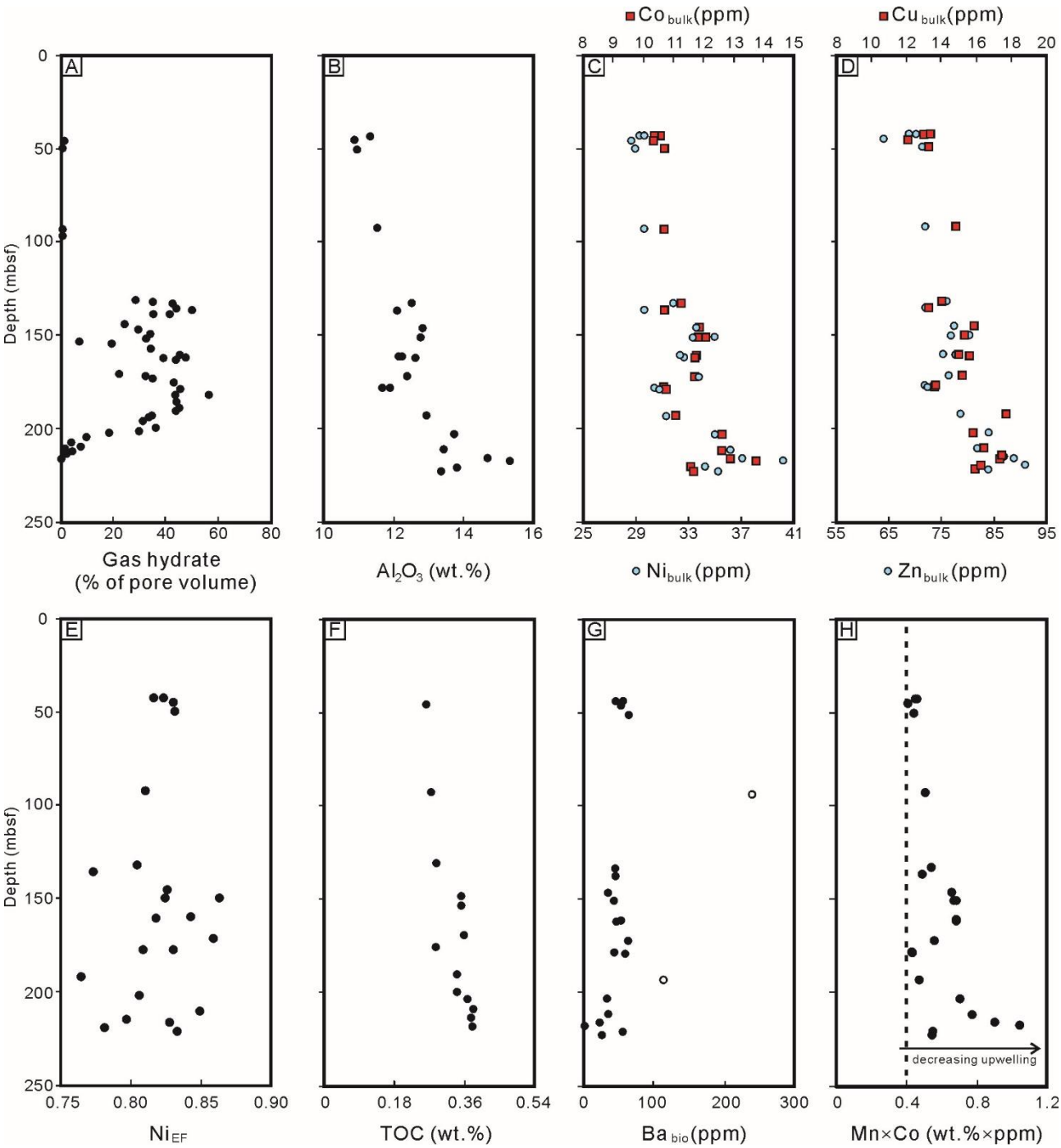

Fig. 3. (A) Gas hydrate concentration (% of pore volume). Data from Yang et al. (2017); (B) Al_2O_3 content (wt. %); (C) Co (red squares) and Ni (blue circles) concentrations of bulk sediments; (D) Cu (red squares) and Zn (blue circles) concentrations of bulk sediments; (E) Ni_{EF}; (F) Total organic carbon (wt.%). Data from Li et al. (2022); (G) Biogenic Ba (ppm). Two samples with open symbols show notably high biogenic Ba compared with other samples; (H) Mn × Co (wt.% × ppm), where the dashed line represents the threshold of 0.4. Mn × Co > 0.4 represents decreased upwelling.

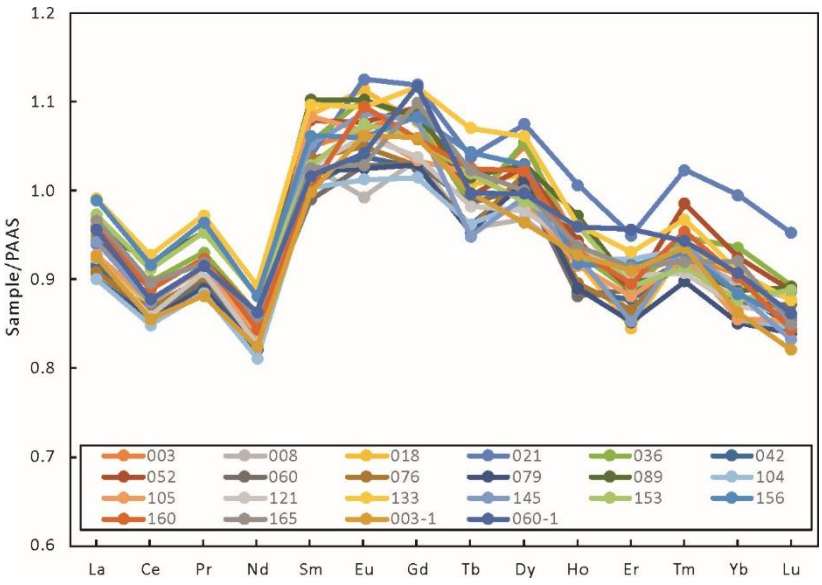

862

863 **Fig. 4.** REE/PAAS of bulk sediments at Site SC03.

864

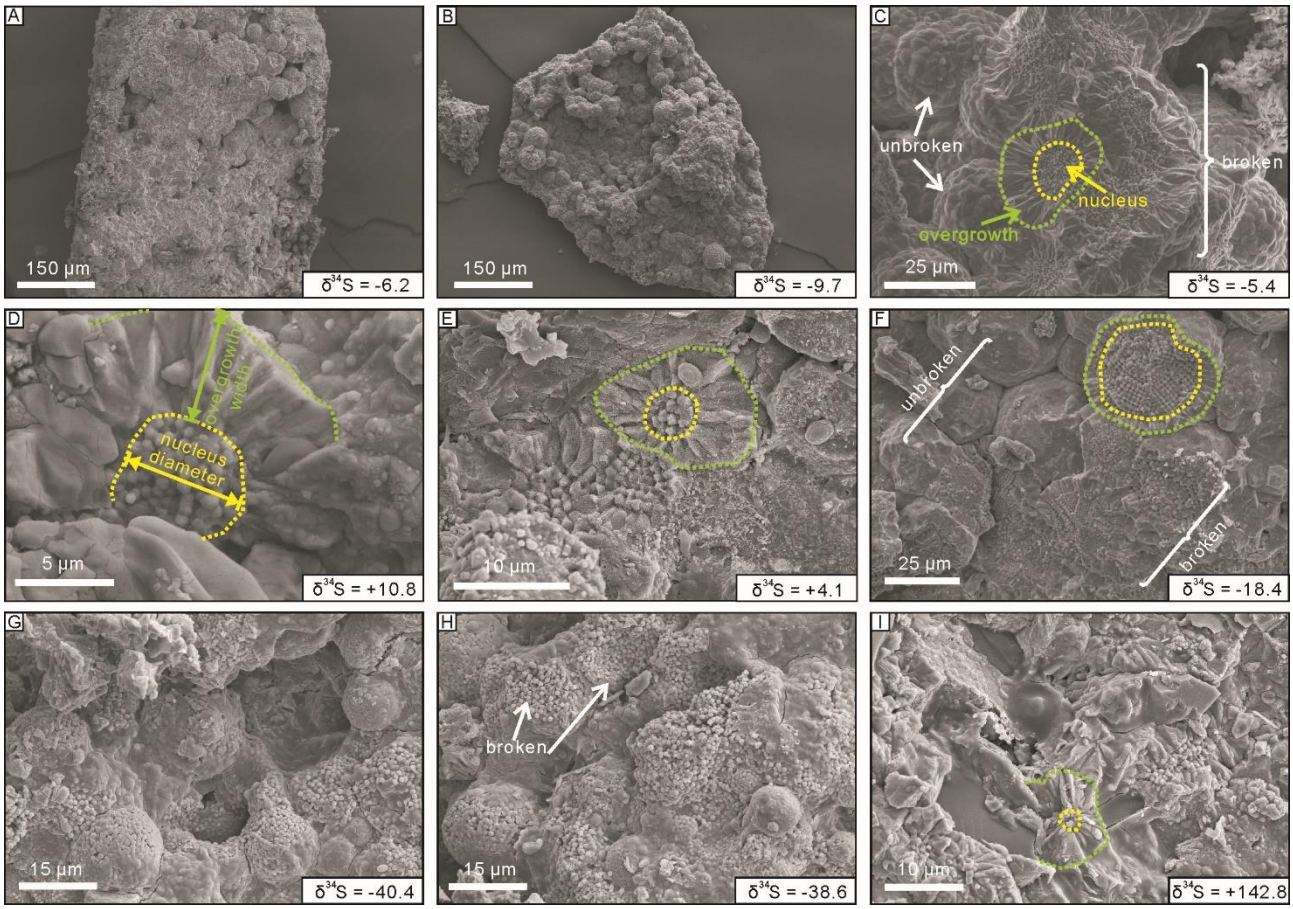

865

866 **Fig. 5.** Scanning electron micrographs of pyrite aggregates at Site SC03. (A) Cylinder-like pyrite
867 aggregates; (B) irregular-shaped pyrite aggregates; (C-E) Broken section of pyrite framboids showing
868 wide radial overgrowths, with some unbroken framboids in C; (F) Broken sections of pyrite framboids
869 showing narrow radial overgrowths, with some framboids in the upper left being unbroken; (G-H)
870 Framboids (broken and unbroken) with no overgrowth; (I) Pyrite aggregates with $\delta^{34}S$ values of up

to +142.8‰. The framboid nucleus and overgrowths are difficult to distinguish.

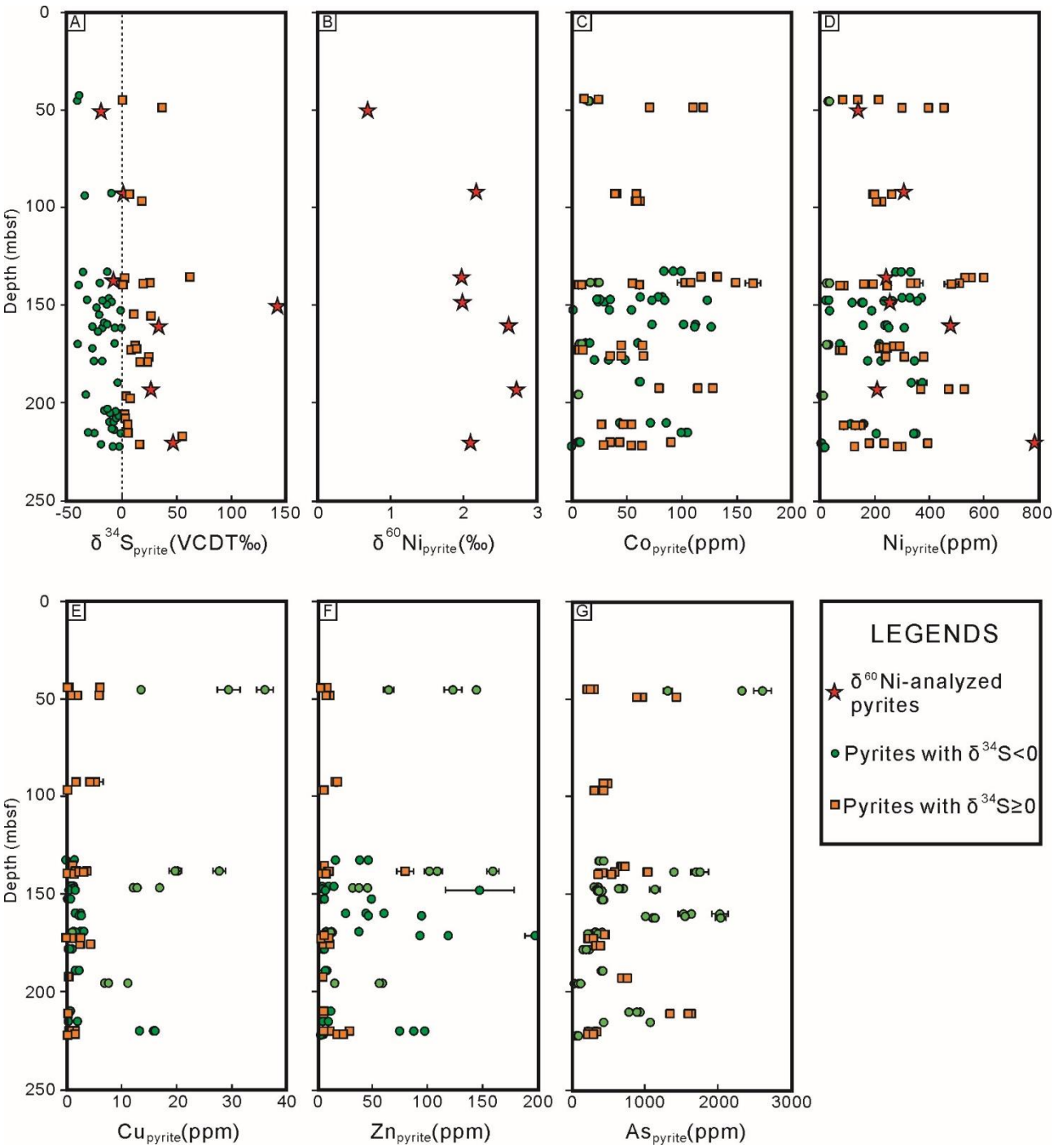

Fig. 6. Sulfur and nickel isotopes and selected trace element compositions of pyrite aggregates at Site SC03. (A) Pyrite sulfur isotopes; (B) Pyrite nickel isotopes; (C) Cobalt concentrations in pyrite aggregates; (D) Nickel concentrations in pyrite aggregates; (E) Copper concentrations in pyrite aggregates; (F) Zinc concentrations in pyrite aggregates; (G) Arsenic concentrations in pyrite aggregates. Red stars represent pyrite aggregates analysed for nickel isotopes. Green circles and red squares represent pyrite aggregates with $\delta^{34}S$ <0‰ and ≥0‰, respectively. Horizontal bars represent 2σ uncertainty in trace-element concentrations (see Table S1).

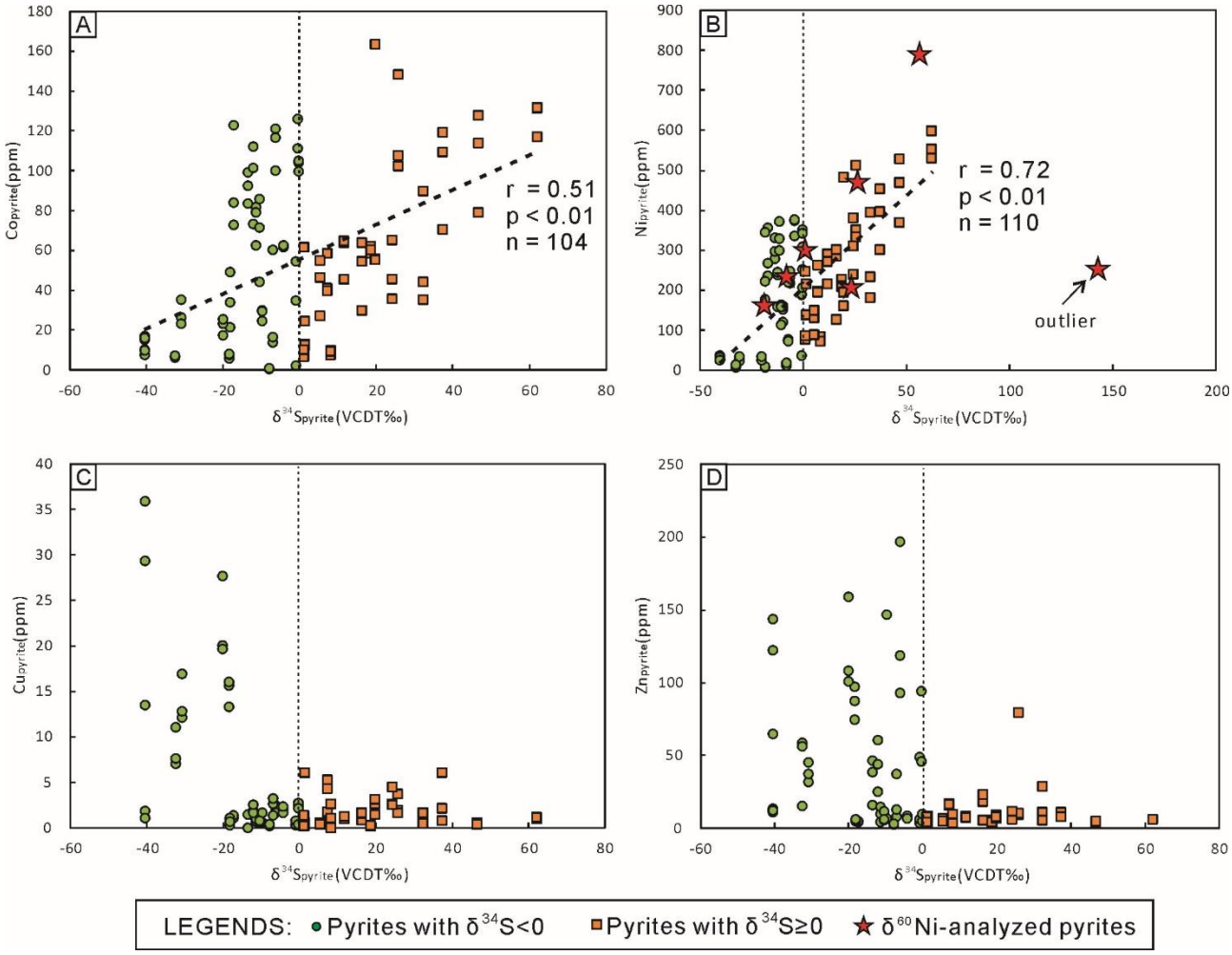

Fig. 7. Cobalt, nickel, copper and zinc concentrations in pyrite aggregates versus pyrite $\delta^{34}S$. *r* in panel B is calculated by excluding one outlier. Symbols are the same as in Fig. 6.

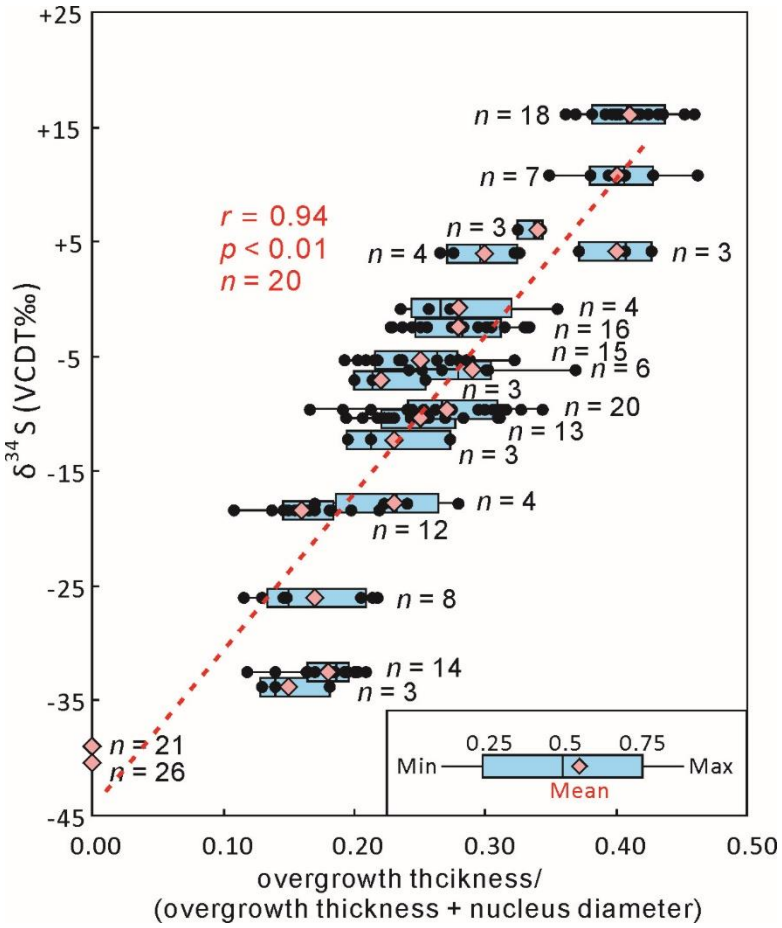

885

886 **Fig. 8.** Pyrite $\delta^{34}S$ vs. framboidal overgrowth thickness/ (overgrowth thickness + nucleus diameter).
887 Samples with a ratio of zero ($\delta^{34}S$ = –38.6‰ and –40.4‰) occur because no overgrowth was evident
888 in SEM images (i.e., Fig. 5G-H). The correlation coefficient (*r*) was calculated based on mean values
889 (pink diamonds).

890

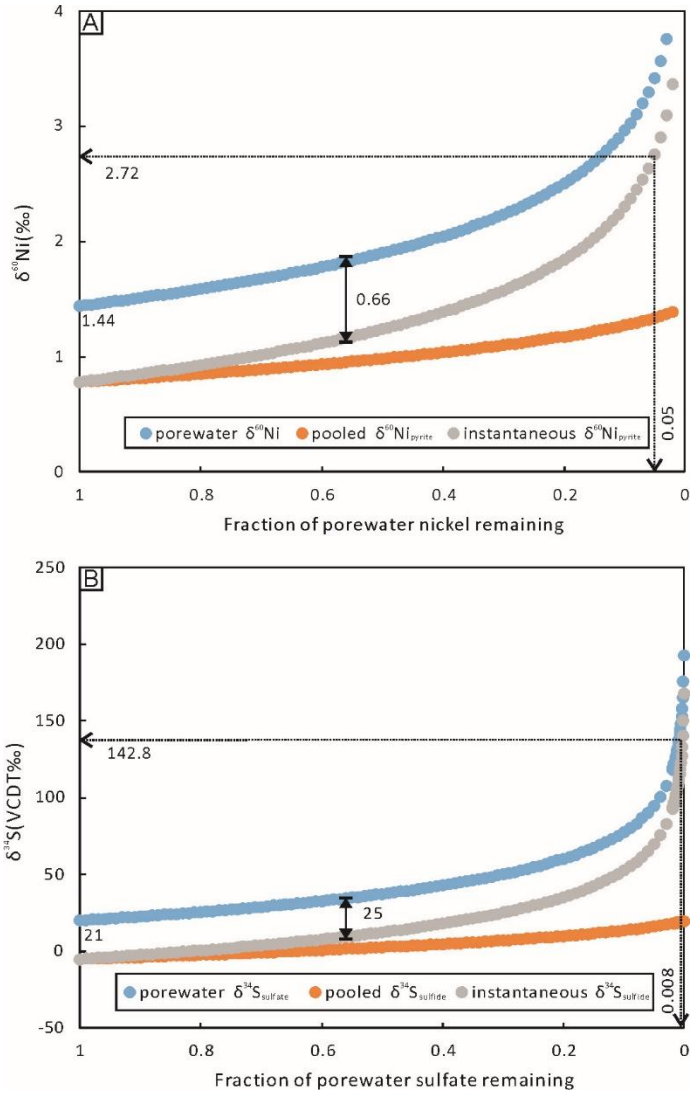

Fig. 9. (A) Schematic showing the isotopic evolution of porewater and pyrite δ^{60}Ni during closed-system nickel uptake by pyrite (with a constant fractionation of –0.66‰); (B) Schematic showing the isotopic evolution of porewater sulfate and sulfide δ^{34}S during closed-system sulfate reduction (with a constant fractionation of –25‰).

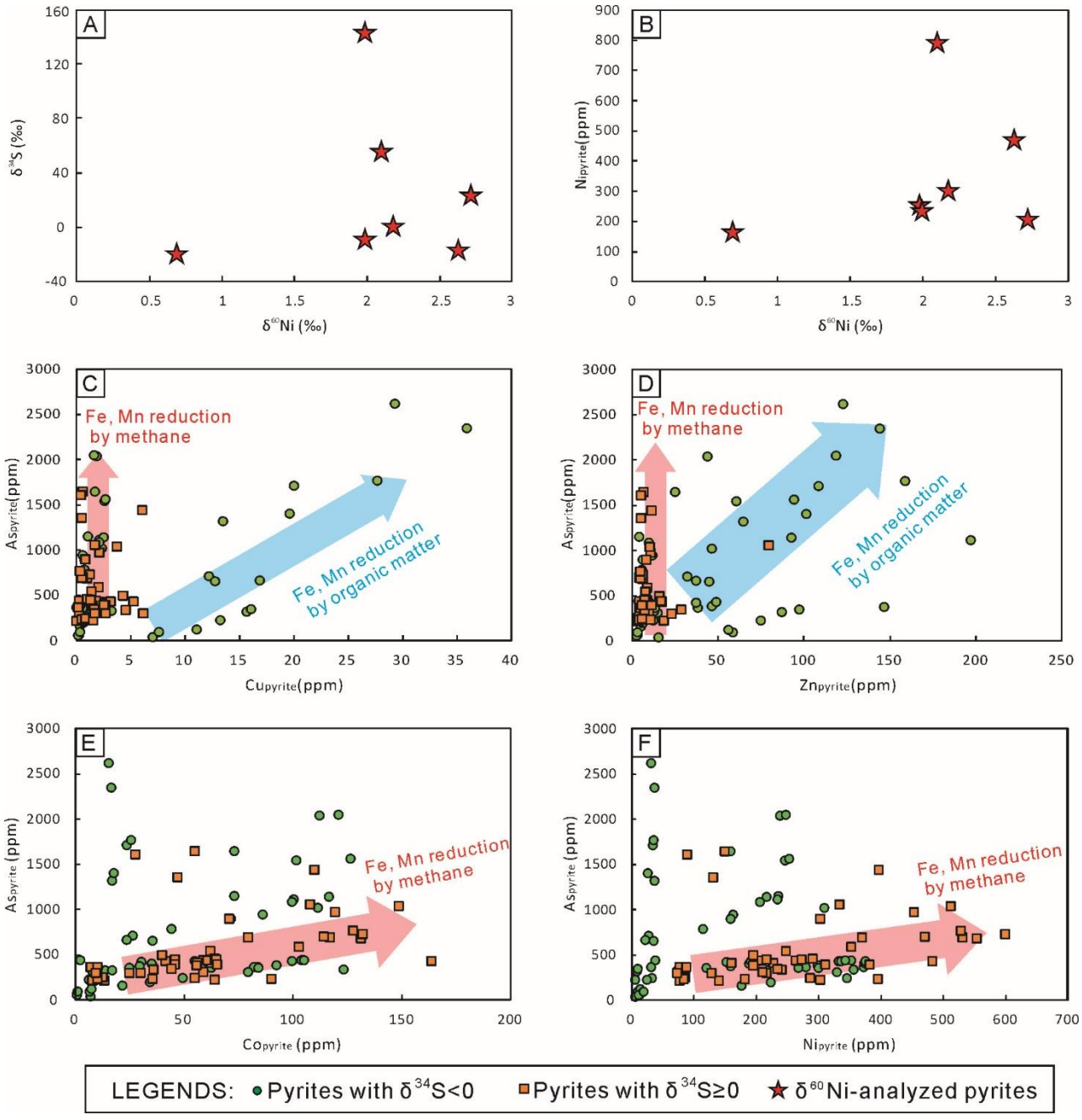

Fig. 10. (A) Pyrite $\delta^{34}S$ vs. $\delta^{60}Ni$; (B) Nickel in pyrite vs. $\delta^{60}Ni$; (C) Arsenic in pyrite vs. copper in pyrite; (D) Arsenic in pyrite vs. zinc in pyrite; (E) Arsenic in pyrite vs. cobalt in pyrite; (F) Arsenic in pyrite vs. nickel in pyrite. Symbols are the same as in Fig. 6.

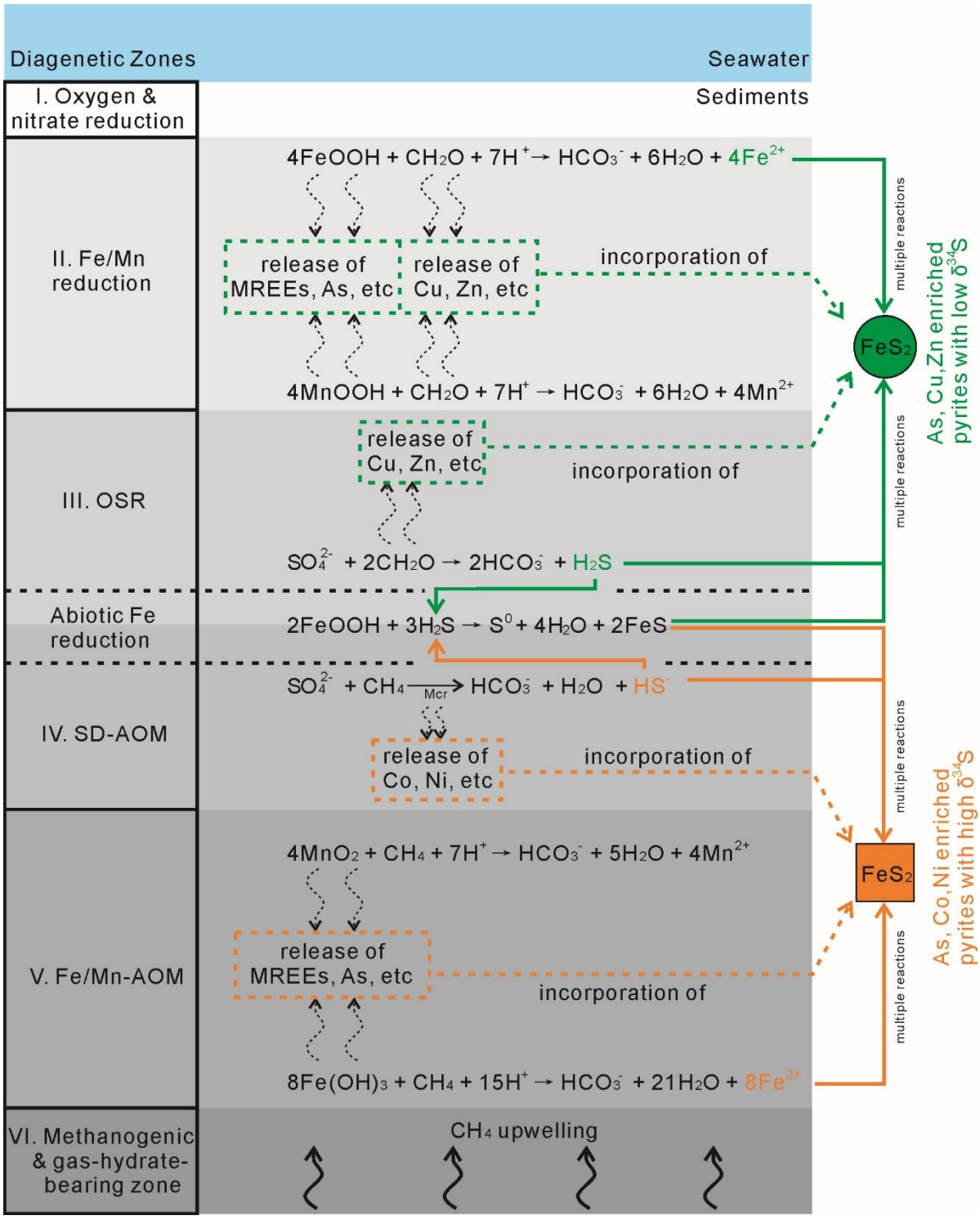

Fig. 11. Schematic model of the uptake of As, Cu, Zn, Co and Ni by pyrite during early diagenesis. Low-$\delta^{34}S$ pyrite formed in the OSR and Fe/Mn reduction zones is enriched in Fe/Mn-(oxyhydr)oxide-released As and organic-mater-released Cu and Zn (green circle, i.e., green circles in Figs. 6, 7 and 10). High-$\delta^{34}S$ pyrite formed in the SD-AOM and Fe/Mn-AOM zones is enriched in Fe/Mn-(oxyhydr)oxide-released As and Mcr-released Co and Ni (orange square, i.e., orange squares in Figs. 6, 7 and 10). Note: Zone V can appear at any depth below Zone II depending on the methane flux and the presence of Fe/Mn-(oxyhydr)oxides.